University of Nevada, Reno

Measurement of thermal accommodation and temperature jump coefficients for stainless steel surfaces and rarefied helium for coaxial cylinders.

A thesis submitted in partial fulfillment of the requirements for the degree of Master of Science in Mechanical Engineering

by

Rachel M. Green

Dr. Miles Greiner/Thesis Advisor

December, 2015

THE GRADUATE SCHOOL

University of Nevada, Reno
Statewide · Worldwide

We recommend that the thesis

prepared under our supervision by

RACHEL GREEN

entitled

Measurement of thermal accommodation and temperature jump coefficients for stainless steel surfaces and rarefied helium for coaxial cylinders.

be accepted in partial fulfillment of the

requirements for the degree of

MASTER OF SCIENCE

Miles Greiner, Ph. D., Advisor

Mustafa Hadj-Nacer, Ph. D., Co-Advisor

Henry Fu, Ph. D., Committee Member

Angelina Padilla, Ph. D., Committee Member

Nicholas Tsoulfanidis, Ph.D., Committee Member

Dev Chidambaram, Ph. D., Graduate School Representative

David W. Zeh Ph.D., Dean, Graduate School

December, 2015

Abstract

The objective of this thesis is to study rarefied gas heat transfer through an annular gap of 1 mm, and to measure the thermal accommodation coefficient at the interface between stainless-steel and rarefied helium. The thermal accommodation and temperature jump coefficients are used to characterize the interaction between gas molecules and wall at the molecular level. It is important to determine its value with precision for better determination of heat transfer at low pressure. The experimental procedure consists of measuring the temperature difference between the inner and outer cylinders as the pressure is decreased in the gap. By measuring the temperature difference and heat flux across the gap the thermal accommodation coefficient can be extracted from the theoretical expression relating the temperature difference to the radial heat flux. Three-dimensional simulations utilizing ANSYS/Fluent commercial code are conducted to determine the legitimacy of the design of the experimental apparatus. These simulations confirmed that the apparatus design is effective to study the heat transfer across rarefied gas and to determine the thermal accommodation coefficient for helium on a stainless steel surface. The comparison between the measured and simulated temperature differences at different pressures, which cover the continuum and slip regimes, enabled the extraction of the thermal accommodation coefficient.

Key words: Heat transfer, rarefied gas, thermal accommodation coefficient, experiment.

Acknowledgments

I would like to take this opportunity to express my sincere gratitude to my advisor Professor Miles Greiner and co-advisor Mustafa Hadj-Nacer, for their relentless support, patience, and guidance through my graduate degree.

I am also very grateful to my colleges: Ernesto Manzo, Dilesh Maharjan, Hasibul Alam, and Corey Trujillo with a special thanks to my friend Jack McCormack.

I am very grateful for all of the support from Soheil Khavandi, who continuously provided the love and encouragement that enabled me to persevere during this journey.

Table of Contents

Nomenclature

A	Boundary surface area [m^2]
c_p	Gas specific heat at constant pressure [J/kg. K]
H	Height [m]
k_b	Boltzmann Constant, 1.38×10^{-23} [m^{2}kg/s^{2}K]
L	Cylinder length [m]
L_c	Characteristic length [m]
m	Molecular mass of the gas [kg]
P	Local pressure [Pa]
Pr	Prandtl number
Q	Heat generation rate [W]
R_A	Inner radius [m]
R_B	Outer radius [m]
R_{cond}	Thermal resistance due to conduction [W/m^2.K]
R_G	Thermal resistance through a gas [W/m^2.K]
R_i	Inner radius [m]
R_{out}	Outer radius [m]
R_S	Thermal resistance through a solid [W/m^2.K]
R_{TJ}	Thermal temperature jump resistance [W/m^2.K]
R_{TJA}	Thermal temperature jump resistance for inner surface [W/m^2.K]
R_{TJB}	Thermal temperature jump resistance for outer surface [W/m^2.K]
T	Temperature [K]
T_A	Hot surface temperature, 330 [K]
T_B	Cold surface temperature, 300 [K]

T_0	Reference temperature, 273.15 [K]
T_g	Temperature of the gas [K]
T_w	Temperature of the wall [K]
V_g	Velocity of gas molecule [m/s]
V_w	Velocity of the wall [m/s]

Greek symbols

α	Thermal accommodation coefficient
κ	Gas thermal conductivity [W/m.K]
λ	Mean free path [m]
λ_d	Mean free path based on the molecular diameter [m]
λ_μ	Mean free path based on the viscosity [m]
μ	Stress viscosity of the gas [kg/ms]
μ_0	Reference viscosity [Pa.s]
γ	Specific heat ratio
ω	Viscosity index
ζ_T	Temperature Jump coefficient

Acronyms

CF	ConFlat
CFD	Computational Fluid Dynamics
DAQ	Data Acquisition/Switch Unit
DSMC	Direct Simulation Monte Carlo
DVM	Discrete Velocity Method
HS	Hard Sphere
ISG	International Standards and Guidelines

NRC   Nuclear Regulatory Committee

SNF   Spent Nuclear Fuel

VHS   Variable Hard Sphere

List of Tables

List of Figures

Chapter I
Introduction

In the United States, the nuclear fuel cycle is referred to as an open or once through fuel cycle [1], because it does not include reprocessing of spent nuclear fuel (SNF). To be able to consider reprocessing in the future, the integrity of the components confining the highly radioactive material [2] should be maintained. This necessity arises due to the harsh conditions that these components experience while in the reactor and during the transport and long-term storage of SNF [3]. Long-term storage has become the temporary solution for handling SNF due to the lack of a safe geological disposal. Reprocessing of SNF would require it to be safely and easily retrievable. Retrievability after decades of storage, partly, depends on the structural integrity of the SNF's cladding, because it is the first barrier of protection against the release of radioactive materials.

1.1. Nuclear fuel assembly

Used fuel rods consist primarily of Zircaloy cladding tubes that contain highly radioactive UO_2 fuel pellets as well as high-pressure fission-product and fill gases [4], as shown in Fig. 1.1 [5]. The fuel rods are held in a square array by headers, footers and periodic spacer plates. Boiling water reactors (BWR) assemblies consist of 7x7 to 9x9 rod arrays surrounded by a Zircaloy channel. Pressure water reactors (PWR) assemblies have 14x14 to 18x18 arrays, but do not have channels.

1.2. Nuclear fuel cycle

The nuclear fuel cycle, shown in Fig. 1.2 [6], explains the progression of nuclear fuel through a sequence of different stages. There are three main stages: the front end, service period, and the back end stages.
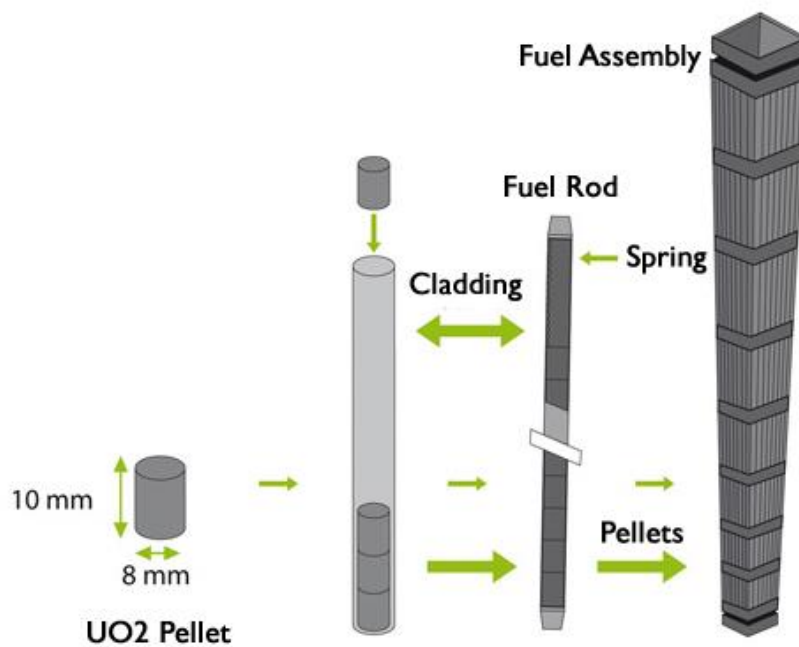
Figure 1.1. Pictorial representation of the composition of used fuel assembly [5].
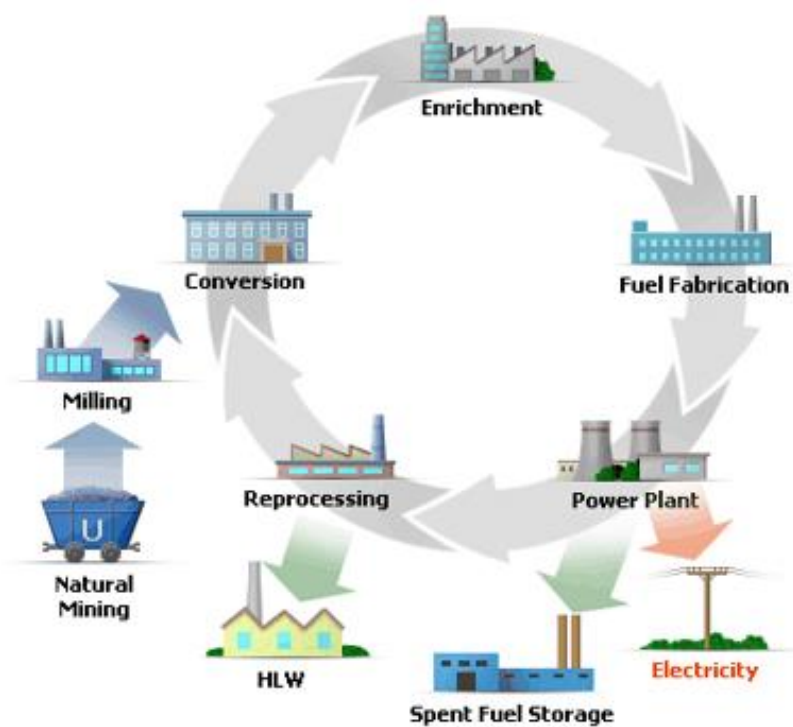
Figure 1.2. Pictorial representation of an open nuclear fuel cycle [6]

First, the front end stage consists of preparing uranium for use in the nuclear reactor, which includes mining, milling, conversion, and enrichment of uranium, and fabrication of the nuclear fuel. Second, the service period stage includes transportation, in-core management, interim storage, reprocessing and many other aspects that directly affect how the nuclear fuel is used during reactor operation. Finally, the back end stage of the fuel cycle is responsible for the safe management of the SNF, which primarily means the removal of SNF from the reactor, storage and/or disposal of the radioactive SNF [1].

1.3. Storage of SNF

The consequence of an open fuel cycle is the rising necessity for long-term storage of SNF. It is possible that the United States will, in the future, consider reprocessing, it is necessary that considerations be made in order to safely retrieve and reprocess the fuel that is in long-term storage.

Preparation for long-term storage starts with removing SNF from the reactor and placing it into a large cooling pool to allow its heat generation and radioactivity rates to decrease to safe levels. After appropriate time, a canister is lowered into the pool and the SNF is placed inside it. The canister is closed, lifted out of the pool and drained. Before the canister is sent for storage, it is subjected to a vacuum drying operation to remove the remaining water and moisture. It is important that all water and moisture be removed to prevent corrosion of the fuel cladding and internal structures, and the creation of a flammable mixture of oxygen and hydrogen within the canister [7]. After drying, the canister is filled with helium to pressures up to 7 atm (711 kPa), sealed, and the final cover lid is bolted or welded in place.

With the absence of a defined used-fuel disposal and/or reprocessing path, it is crucial to ensure the safety of long-term dry cask storage systems [2, 36]. Federal regulations (10CFR72) requires that "spent fuel cladding must be protected during storage against

degradation that leads to gross ruptures or the fuel must be otherwise confined such that degradation of the fuel during storage will not pose operational safety problems with respect to its removal from storage," [36]. The cladding is the primary confinement barrier for the used fuel pellets and fission gas. Its integrity must be protected to ensure that, after decades in storage, the SNF can be safely transferred to other packages, and/or transported to other locations, [36]. Radial hydride formation within the cladding has the potential to radically reduce cladding ductility and its suitability for transport or long-term storage. During all post-reactor, drying, transfer, storage and transport operations, the fuel cladding must be kept below the temperature limit of 400℃ (673K), specified by the Nuclear Regulatory Commission (NRC) Interim Stagg Guidance-11, Revision 3 (ISG-11) [7, 36], to avoid (a) dissolution of circumferential hydrides that exist in the cladding and (b) high gas pressures within the tubes, which leads to high cladding hoop stress [8]. If these hydrides dissolve and the hoop stresses become large, then as the heat generation of the used fuel decreases during long-term storage radial hydrides may form and cause the cladding to become brittle [8-11]. Vacuum drying operation [12] one of the events to most likely cause the fuel temperature to exceed the temperature limit. This is because it is the first operation when the fuel is removed from water and placed in a gas-filled environment, while the fuel heat generation is still relatively high.

1.4. Vacuum drying

During vacuum drying operation, the pressure in the canister is decreased to as low as 67Pa to promote evaporation and removal of remaining water [13]. Several cycles of evacuation and refill are required before the operator can demonstrate that the canister satisfies the technical specifications of maintaining pressure of 400 Pa (3 Torr) for 30 minutes [14]. Because of the low pressures and densities associated with vacuum drying, buoyancy-induced gas motion and natural convection heat transfer within the helium gas

can be neglected. The thermal conductivity of the gas is almost the same as it is at atmospheric conditions. Moreover, the rarefaction condition (low pressure) induces a notable temperature difference (temperature jump) at the interface between wall surfaces and gas [15]. As the pressure decreases, this temperature jump increases and causes the cladding temperature to increase.

1.5. Temperature jump

The temperature jump is characterized by the thermal accommodation coefficient [15, 16]. At low pressure the collisions between gas molecules and the surfaces dominate the molecules-molecules collisions. In these conditions, the continuity of the macroscopic parameters (velocity and temperature) near the walls are not achieved. The concept of the accommodation coefficient was, first, introduced by Maxwell during the mid-nineteenth century [17]. The thermal accommodation coefficient (α) is related to the temperature of incident T_i and reflected T_r molecules as

$$\alpha = \frac{T_i - T_r}{T_i - T_w} \quad , \tag{1}$$

where T_w is the wall temperature. The value of α varies from 0 to 1. In the case $\alpha=0$, the molecules are reflected specularly, without transferring any of their momentum or energy to the surface (the molecule's temperature and velocity components parallel to the wall remain unchanged, but the velocity component normal to the wall is reversed). For $\alpha=1$, the molecules are reflected diffusely; a molecule leaving the surface "forgets" all information upon collision and leaves accommodating the surface properties (i.e., their average bulk velocity is equal to the surface velocity and their temperature is equal to the temperature of the surface). A lower value of α leads to a higher temperature jump between the wall and gas molecules interacting with it.

The values of α were experimentally determined for a wide range of surfaces and gas molecules by using different methods [18]. Its value depends on a number of parameters, such as the type of gas, surface material, its cleanliness and its roughness. Authors [19, 20] reported values of α close to 1 for heaviest molecules and smaller values for lighter molecules. The value of α reported for the pair helium-stainless steel [18-22] is in the range [0.2, 0.4] for T=700K to 300K.

1.6. Objective

The long term objective of the current research is to develop and experimentally benchmark computational models that predict the temperature difference between the cladding and basket walls during vacuum drying operations. An experimental apparatus that consists of 7×7 array of heated rods enclosed in square-cross-section-pressure-vessel subjected to vacuum conditions will be constructed by another investigator. The measurements will be compared to the computational model that will include the temperature jump boundary condition at the gas/surface interfaces.

The goal of this thesis is to experimentally observe the rarefaction effect on heat transfer and measure the temperature jump and thermal accommodation coefficients between stainless-steel and helium gas. To achieve this goal, an experimental apparatus that consists of two coaxial cylinders spaced by a 1 mm gap is constructed. The temperature of the outer cylinder is controlled and the inner cylinder is heated using a cartridge heater. Decreasing the pressure between the cylinders will allow the temperature of the inner cylinder to increase due to the rarefaction effect. Using a theoretical expression that relates the heat flux across the cylinders to the pressure and temperature difference between the cylinders, the temperature jump and thermal accommodation coefficients can be deduced. Three dimensional simulations were performed using ANSYS/Fluent package to accurately represent the experimental apparatus. Conduction and radiation heat transfer

simulations were performed with rarefied helium gas filling the gap region between the coaxial cylinders. The temperature of the outer cylinder is maintained at a constant value of 300K and the pressure is varied from 10^5 to 200 Pa. These simulations allowed the validation of the experimental apparatus design.

1.7. Thesis structure

The first chapter presents a brief introduction to the problem covered in this thesis, where a description of the nuclear fuel assembly and cycle are given. The problem related to storage and drying process of the nuclear fuel canister is also presented. The effect of rarefaction and temperature-jump on the increase of SNF temperature is briefly introduced. The second chapter discusses the theory behind the rarefaction effects and how these effects are implemented in ANSYS/Fluent and benchmarked with analytical results in order to validate its application for this thesis work. The third chapter presents a detailed description of the experimental apparatus design and construction, component specifications, and dimensions are listed here along with preliminary testing procedures. The fourth chapter discusses the obtained experimental data and compares them to the predicted results from ANSYS/Fluent. Lastly, the thesis conclusion is found in the fifth chapter that summarizes the findings.

Chapter II
Theory and numerical modelling

During vacuum drying operation, the pressure in the canister can be as low as 67 Pa to promote evaporation and water removal. At this level of pressure, the gas is rarefied and the heat transfer through the gas is reduced compared to the atmospheric conditions, which makes the study of the rarefaction effect very important because it can make the cladding temperature exceed the limit specified by ISG-11 [7].

When the gas rarefaction increases, the importance of the gas-surface collisions increases in comparison to the gas-gas collisions; therefore, the gas cannot reach the equilibrium state with a surface and the difference between the surface and the gas temperatures (temperature jump) becomes essential. Therefore, it is very important to know the characteristics of the gas-surface collisions, especially the temperature jump and thermal accommodation coefficients, which may depend on the surface properties (such as the surface material, temperature, roughness, contaminants, etc.) and the gas nature.

2.1. Mean free path

The mean free path is the average distance that molecules travel between successive collisions, which could change the particles direction or energy. Many different definitions can be found in literature for the mean free path [23], however, for our applications, only one definition is retained in this thesis

$$\lambda = \frac{\mu}{P}\sqrt{\frac{2k_B T}{m}} \, , \tag{2.1}$$

where P is the pressure, T is the temperature, k_B is Boltzmann's constant, m is the molecular mass of the gas, and μ is the dynamic viscosity, whose temperature dependence is defined as

$$\mu = \mu_0 \left(\frac{T}{T_0}\right)^{\omega}.$$
(2.2)

In the above expression, μ_0 is the reference dynamic viscosity calculated at the reference temperature $T_0=273.15$ K, and its value depends on the gas nature. For helium $\mu_0=1.865\times10^{-5}$ Pa.s. The coefficient ω depends on the molecular interaction model and is equal to ½ for the Hard Sphere (HS) model, and is dependent on the gas nature for Variable Hard Sphere (VHS) model. In this thesis, only the HS model is retained for calculations of the gas viscosity.

2.2. Rarefaction regimes

As the pressure and/or size of a container decrease, the effect of rarefaction increases. This effect can be characterized using the Knudsen number, which is defined as the ratio between the mean free path, λ (2.1), and a characteristic length, L_c. Typically, this length scale represents the smallest length in the container, such as radius of tube or cross sectional length of a channel. The Knudsen number is defined as

$$Kn = \frac{\lambda}{L_C}.$$
(2.3)

The Knudsen number is used as a parameter to describe the gas rarefaction level. As this number increases, the gas becomes more rarefied. This happens when the mean free path λ increases (i.e. in case of pressure decreasing) or when the characteristic length L_c decreases. In the case of an SNF canister, there are many gaps that can be considered as characteristic lengths; the peripheral gap between the basket support and the canister enclosure, the gap between the fuel rods and the basket, and the gap between the fuel rods.
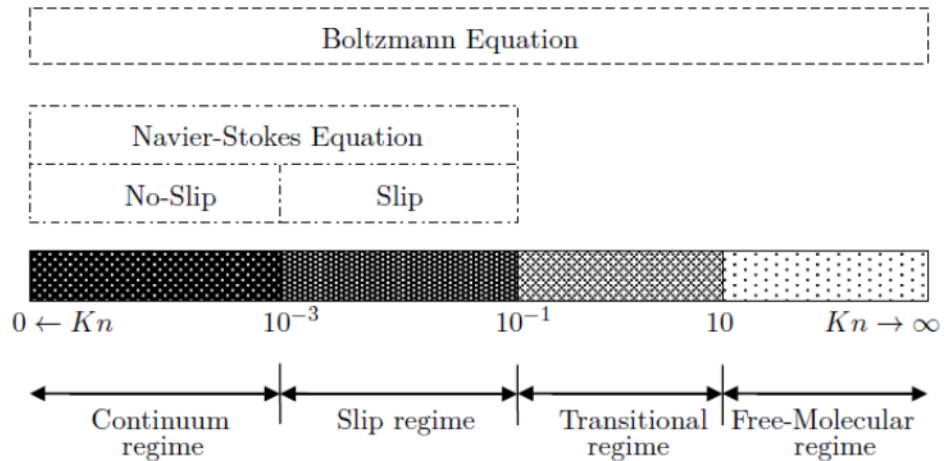
Figure 2.1. Flow regimes categorized by the Knudsen number [24].

For a simple two concentric cylinders geometry, the gap between the cylinders can be considered as the characteristic length.

Schaaf and Chambre [15] suggested to use the Knudsen number as guidelines for identifying different rarefied gas regimes (see Figure 2.1). Usually, the following classification is used:

- Continuum regime ($Kn \leq 10^{-3}$), where the flow and heat transfer are modeled accurately using the Navier-stokes and Convective Energy equations, along with traditional no-slip boundary conditions at the solid-fluid interface.

- Slip regime ($10^{-3} \leq Kn \leq 10^{-1}$), where the continuum model (Navier-Stokes and Convective Energy equations) can still be applied away from the wall, however, the velocity slip and temperature jump boundary conditions must be employed at the walls. In this regime, the gas is considered to be moderately rarefied.

- Transitional regime ($10^{-3} \leq Kn \leq 10^{-1}$), where the continuum model (Navier-Stokes and Convective Energy equations) is no longer valid and instead the Boltzmann equation should be solved using the Discrete Velocity (DVM) or Direct Simulation Monte Carlo (DSMC) methods.

- Free molecular regime ($Kn \leq 10$), where the flow is highly rarefied. In this regime the number of molecule-molecule collisions are smaller than the numbers of molecule-surface collisions. Therefore, transport is driven by the interaction between gas and wall. The flow and heat transfer, in this case, are modeled using the numerical solution of collisionless kinetic Boltzmann equation or DSMC method.

The limits defining the boundaries of the different regimes, shown in Fig. 2.1, are to be taken as an order of magnitude. The transition between regimes is not precise but progressive. All the regimes discussed above can be accurately modeled using the kinetic theory, by solving the Boltzmann equation. Nevertheless, it is inefficient to implement this equation or other kinetic equations for gas flow simulation in the continuum and slip regimes because of the large computational efforts needed for their solution.

2.3. Temperature jump effect

Regarding the pressures during vacuum drying operation and the characteristic length of the SNF canister, the gas is in the slip regime. For this reason, only the continuum and slip regimes are considered in this thesis.

As mentioned previously, when the gas is in the slip regime, it is considered to be moderately rarefied [15]. In such case, the gas tends to behave as a continuum in regions away from the walls. However, a molecule that comes into contact with a wall does not meet other molecules enough times to reach equilibrium with them and the wall [16], [25], *i. e.* there is a discontinuity of temperature and velocity near the wall ($T_g \neq T_w$, and $V_g \neq V_w$), called temperature jump or velocity slip. As seen above, when in the slip regime ($10^{-3} \leq Kn \leq 10^{-1}$), the Navier-Stokes and Convective Energy equations can accurately model momentum and energy transport away from the walls, however, near the walls, temperature jump effect must be considered using the "temperature-jump" and "velocity-slip" boundary conditions [15, 16].

Smoluchowski (1898) [26] proposed an expression of first order for the temperature jump boundary condition as

$$T_g - T_w = \zeta_T \lambda \left. \frac{\partial T}{\partial y} \right|_w ,$$
(2.4)

where T_g is the temperature of the gas near the wall and T_w is the temperature of the wall. ζ_T, in above equation, is the temperature jump coefficient. Kennard [27] proposed an expression for this coefficient

$$\zeta_T = \frac{2 - \alpha}{\alpha} \frac{\sqrt{\pi} \gamma}{(\gamma + 1) \mathrm{Pr}},$$
(2.5)

by assuming that the incident gas molecules on the surface have the same distribution function as the molecules in the bulk of the gas. In expression (2.5), Pr is the Prandtl number and γ is the ratio of specific heats. Welander [28] proposed another expression for monatomic gas, which was generalized for polyatomic gases by Lin and Willis [29], who used the BGK (Bhatnagar-Gross-Krook) model to resolve the Boltzmann equation. This expression reads

$$\zeta_T = \left(\frac{2 - \alpha}{\alpha} + 0.17 \right) \frac{\sqrt{\pi} \gamma}{(\gamma + 1) \mathrm{Pr}} .$$
(2.6)

By using the Linearized Boltzmann equation Loyalka found an expression for the temperature-jump coefficient for monatomic gases as

$$\zeta_T = \frac{15 \sqrt{\pi}}{16} \left(\frac{2 - \alpha}{\alpha} \right) (1 + 0.1621 \alpha) .$$
(2.7)

The use of the different models, given above, for temperature-jump coefficient gives different values of ζ_T for a given value of the thermal accommodation coefficient. Table 2.1 shows the values of the temperature-jump coefficient ζ_T for the values of thermal accommodation coefficient considered in this thesis α=1, 0.4, and 0.2. It can be seen from

this table that the Lin & Willis and Loyalka models give close results, however, the Kennard model gives lower values. The difference between the Kennard model and the other models decrease as the value of α decreases. In this thesis, the Lin & Willis model is retained for the calculation of the temperature-jump coefficient. The reason for this choice will be explained in Sec. 2.5.

Table 2.1. Temperature Jump Coefficient values for different models and thermal accommodation coefficients

Temperature Jump models	ζ_T		
	$\alpha = 1$	$\alpha = 0.4$	$\alpha = 0.2$
Kennard	1.66	6.65	14.96
Lin & Willis	1.94	6.93	15.24
Loyalka	1.93	7.08	15.44

2.4 Modeling the temperature jump effect

The temperature jump effect at the interface between the wall and gas can be modeled as a resistance. Expression (2.4) can be re-written in the following form

$$T_g - T_w = R_{TJ}Q . \tag{2.8}$$

In this model, Q is the portion of the heat transfer rate directed to the solid surface and transported by conduction within the surrounding gas and does not include the component transported by radiation to other surfaces, [36]. The temperature jump thermal-resistance is

$$R_{TJ} = \frac{\lambda \zeta_T}{A\kappa} . \tag{2.9}$$

In this expression, A is the boundary surface area and κ is the gas thermal conductivity that is related to the viscosity μ (Eq. 2.2), the gas specific heat at constant pressure c_p, and Prandtl number Pr as

$$\kappa = \frac{c_P}{\text{Pr}}\mu . \tag{2.10}$$

In equation (2.9), ζ_T is the temperature jump coefficient, whose definition is given in Eq. 2.4.

To better understand how this resistance is applied to the Navier-Stokes and Convective heat transfer equations, let us consider heat being transferred through an interface between a solid and a gas, as shown in Fig. 2.2.
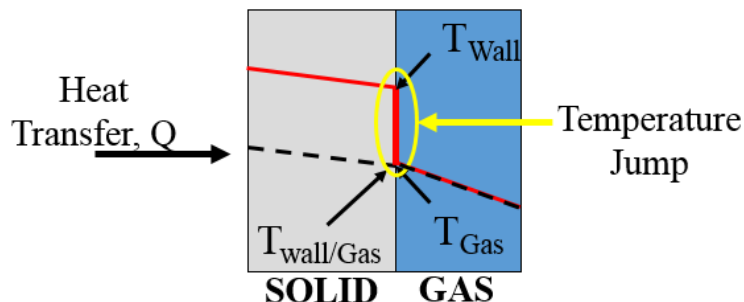
Figure 2.2. Pictorial representation of heat transfer through a solid and then a gas.

From this figure, it can be seen that in the case of continuum condition (dashed line), the gas and solid temperatures at the interface are equal, *i.e.* $T_g = T_w$. However, when the gas is moderately rarefied (solid line), in the slip regime, these temperatures are different, *i.e.* $T_g \neq T_w$, which represents the temperature jump.

From Fig. 2.2, the heat transferred through the solid, the interface, and then the gas can be written as a sum of resistances as the following,

$$Q = \frac{\Delta T}{\sum R}, \tag{2.11}$$

where,

$$\sum R = R_S + R_{TJ} + R_G. \tag{2.12}$$

R_S and R_G represent the resistances through the solid and gas, respectively, and R_{TJ} (2.9) is the thermal temperature-jump resistance at the interface gas/solid.

2.5 Numerical modeling using ANSYS/Fluent

ANSYS/Fluent computational fluid dynamic (CFD) package utilizes a simplified model to predict the temperatures at the interfaces between rarefied gases and solid surfaces. This is accomplished by using an equation similar to (2.4). The key difference is that it employs a different expression for the temperature jump coefficient that does not include gas parameters, written as

$$\zeta_T = 2\left(\frac{2-\alpha}{\alpha}\right), \tag{2.13}$$

This expression is different from expressions (2.5) and (2.6) by the factor $\sqrt{\pi}\gamma/\left((\gamma+1)\mathrm{Pr}\right)$ which is assumed in equation (2.13) to be equal to 2. In order to implement expressions (2.5) – (2.7) in ANSYS/Fluent, a User Define Function can be used. For all ANSYS/Fluent simulations carried out in this thesis, the Lin and Willis temperature jump coefficient (2.6) will be used due to it is in very good agreement with the kinetic simulations that were carried out using the Shakhov model (S-model) kinetic equation. Further, detail as to the justification for using the Lin and Willis model can be found in [30].

2.6. Benchmark of ANSYS/Fluent

To check the ability of ANSYS/Fluent to reproduce the same results as the analytical expressions given in sections 2.3 and 2.4, simple two-dimensional parallel plates and coaxial cylinders geometries are created, as shown in Fig. 2.3. For the planar region (Fig. 2.3a), the gap H between the parallel plates is 1 cm and the length L is set to 100 times the height H in order to neglect the lateral walls effect. For the annular region (Fig. 2.3b) the radii of the inner and outer cylinders are R_A=0.5 cm and R_B=1.0 cm, respectively. The hot and cold temperatures of the surfaces for both geometries are respectively, T_A=330°C and T_B=300°C (see Figure 2.3).
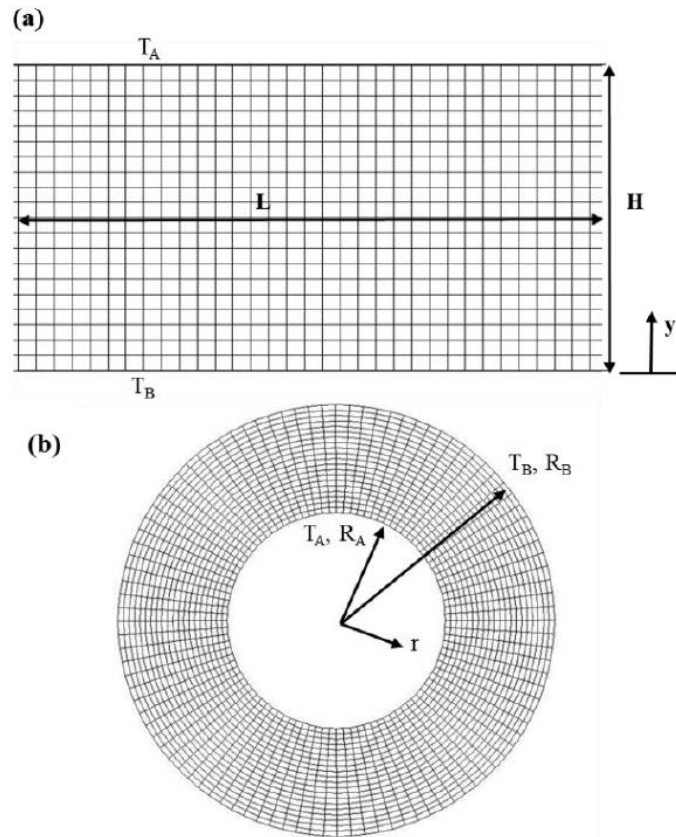
Figure 2.3. Benchmark Computational Domains (a) planar region between parallel plates, domain composed of 42,000 nodes and 40,000 elements   (b) annular region between coaxial cylinders, domain composed of 2100 nodes and 2000 elements.

In order to benchmark the ANSYS/Fluent simulations comparison with the simple analytical model based on the Lin and Willis temperature jump model for parallel plates and coaxial cylinders was performed.

The heat flux was calculated for several gas types and temperature difference between parallel plates and the coaxial cylinders using the Lin and Willis temperature jump model (Eq. 2.6). For the analytical model the conduction heat transfer Q is calculated by applying Eq. 2.11 as

$$Q = \frac{T_H - T_C}{R_{TJ_A} + R_{Cond} + R_{TJ_B}}, \qquad (2.14)$$
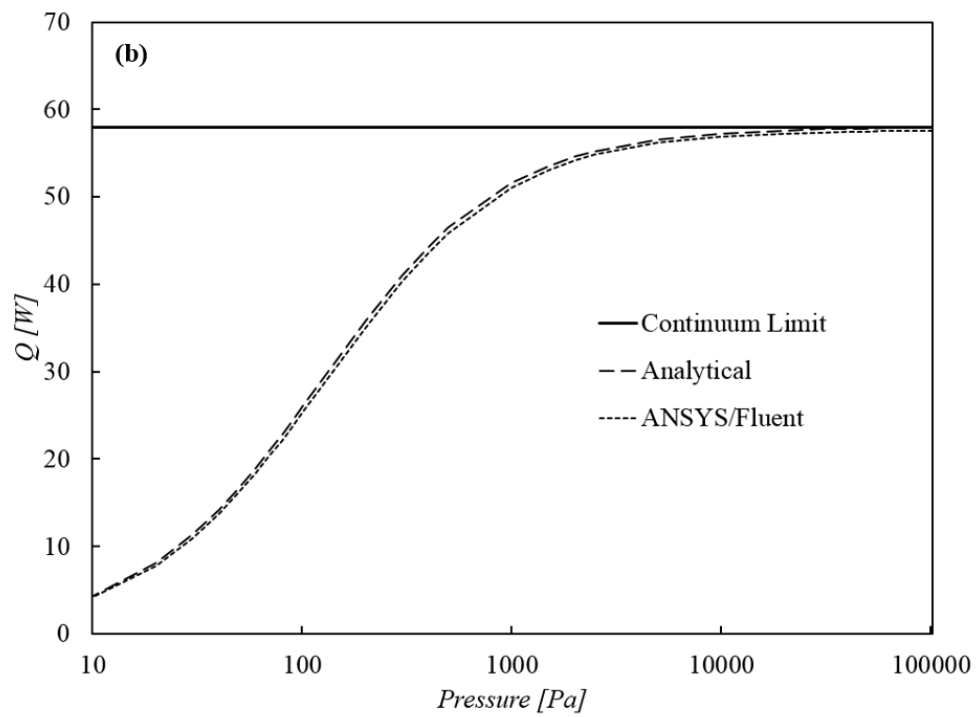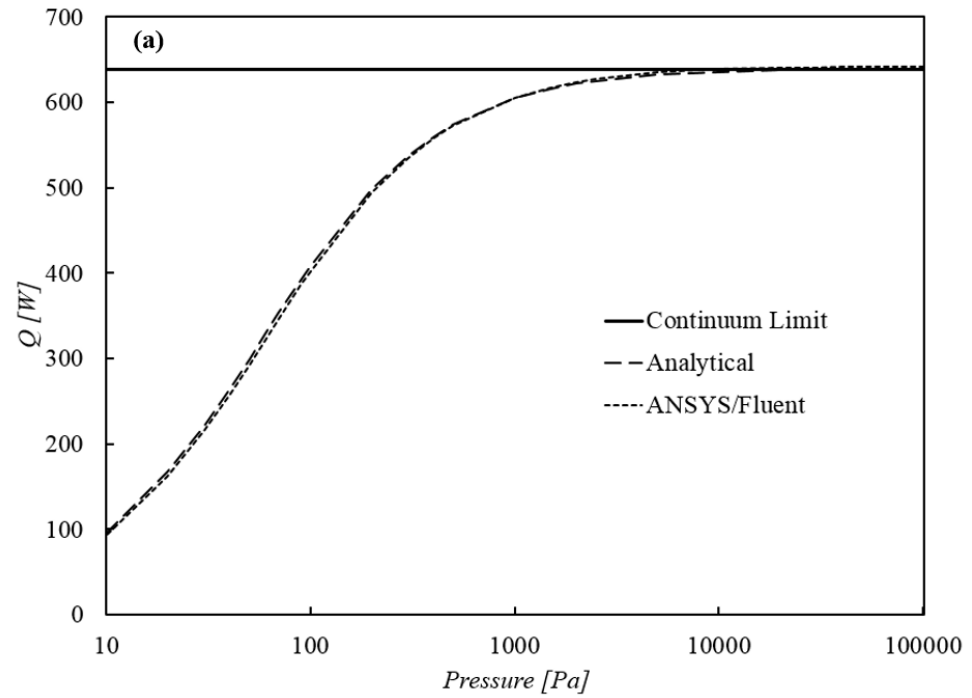
Figure 2.4. Heat flux versus pressure for (a) planar region between parallel plates and (b) annular region between coaxial cylinders.

where R_{Cond} is the thermal resistance associated with conduction within the helium while R_{TJ_A} and R_{TJ_B} are the temperature-jump thermal resistances for the hot and cold surfaces, respectively.

Figure 2.4 shows the conduction heat transfer versus pressure for ANSYS/Fluent simulations and the analytical model that uses the Lin & Willis temperature-jump coefficient model for the planar region (Fig. 2.4a) and the coaxial cylinders (Fig. 2.4b). The thick horizontal solid line in Figs. 2.4a and 2.4b shows the heat flux calculated for the continuum condition (atmospheric pressure) using equation (2.14) with temperature-jump-thermal-resistance R_{TJ_A} and R_{TJ_B} set to zero, while the dashed lines show the ANSYS/Fluent model and analytical model for $\alpha = 0.4$. From Fig. 2.4a and 2.4b, one can see that the Fluent model was able to predict with good accuracy the conduction heat transfer from moderate low pressure to atmospheric conditions for both parallel plates and coaxial cylinders.

Chapter III
Experimental Apparatus

The main objective of this thesis is to experimentally observe the effect of rarefaction on heat transfer through an annular gap between two coaxial cylinders and to measure the temperature jump and the thermal accommodation coefficients at the interface between stainless steel and helium. Many researchers, in the literature, have measured the thermal accommodation coefficient in both parallel plates and coaxial cylinders geometries [32-36]. This thesis is a contribution to this domain. The main differences with previous works is the very small aspect ratio (R_{out}/R_{in}) between the coaxial cylinders used in this work and the focus on the continuum and slip regimes while previous works obtained the thermal accommodation coefficient in the transitional and free molecular regimes.

Recently, the research on rarefied gases and thermal accommodation coefficient became very important, especially in the field of micro and nano technologies. This importance raises due to the small dimensions involved in these devices. The most recent works on the measurement of thermal accommodation coefficient are the works of Trott et *al*, 2011 [19] and Yamaguchi et *al*, 2012 [20]. In both works the thermal accommodation coefficient was obtained using the relation between the pressure and the conductive heat flux.

Trott et *al* [19], from Sandia National Laboratories, Albuquerque, New Mexico, obtained the thermal accommodation coefficient in the free molecular regime by measuring heat flux through parallel plates geometry. They applied a formula based on DSMC simulations to calculate this coefficient. Experiments were performed for varying surface materials, roughness, and contamination. The important aspect of Trott's et *al* work for this thesis is that they conducted

experiment for 304 stainless steel surface and helium gas, which is also used in this work. Their results showed that for helium and stainless steel surface, the thermal accommodation coefficient is ~0.46 for engineering surface and ~0.38 for cleaned surface.

Yamaguchi et *al* [20], from the Department of Micro-Nano Systems Engineering, Nagoya University, Japan, used the low-pressure method to obtain the thermal accommodation coefficient between two coaxial cylinders having different surface materials (Pyrex glass and platinum wire). They measured the heat flux in the free molecular to the early transitional regimes and calculated the value of the thermal accommodation coefficient for argon gas. For their experimental setup, a large aspect ratio and a large temperature difference were implemented. They reported value of thermal accommodation coefficient ranging from 0.682 to 0.876 depending on temperature.

3.1. Experimental apparatus

As it was mentioned above, the objective of the experimental apparatus is to observe the effect of rarefaction and to measure the temperature jump and the accommodation coefficients. To achieve this objective, two possible geometries can be adopted, the parallel plates or the coaxial cylinders. For both of these simple geometries, theoretical expressions that relate the heat flux and temperature to the pressure can be found in the literature. In current work, the coaxial cylinders geometry was chosen. This choice was motivated due to the ability to construct coaxial cylinders could be accomplished without needing more resources.

The experimental setup consists of a simple two coaxial cylinders spaced with a gap of 1 mm. The inner cylinder is heated while the outer cylinder's temperature is controlled. The dimensions of the apparatus were chosen to:

- Attain the limit between the slip and transitional regimes ($Kn = 0.1$) with reasonable low pressure ($P \approx 200$ Pa). It was mentioned before that during vacuum drying operation of SNF canister, helium is within the slip regime.
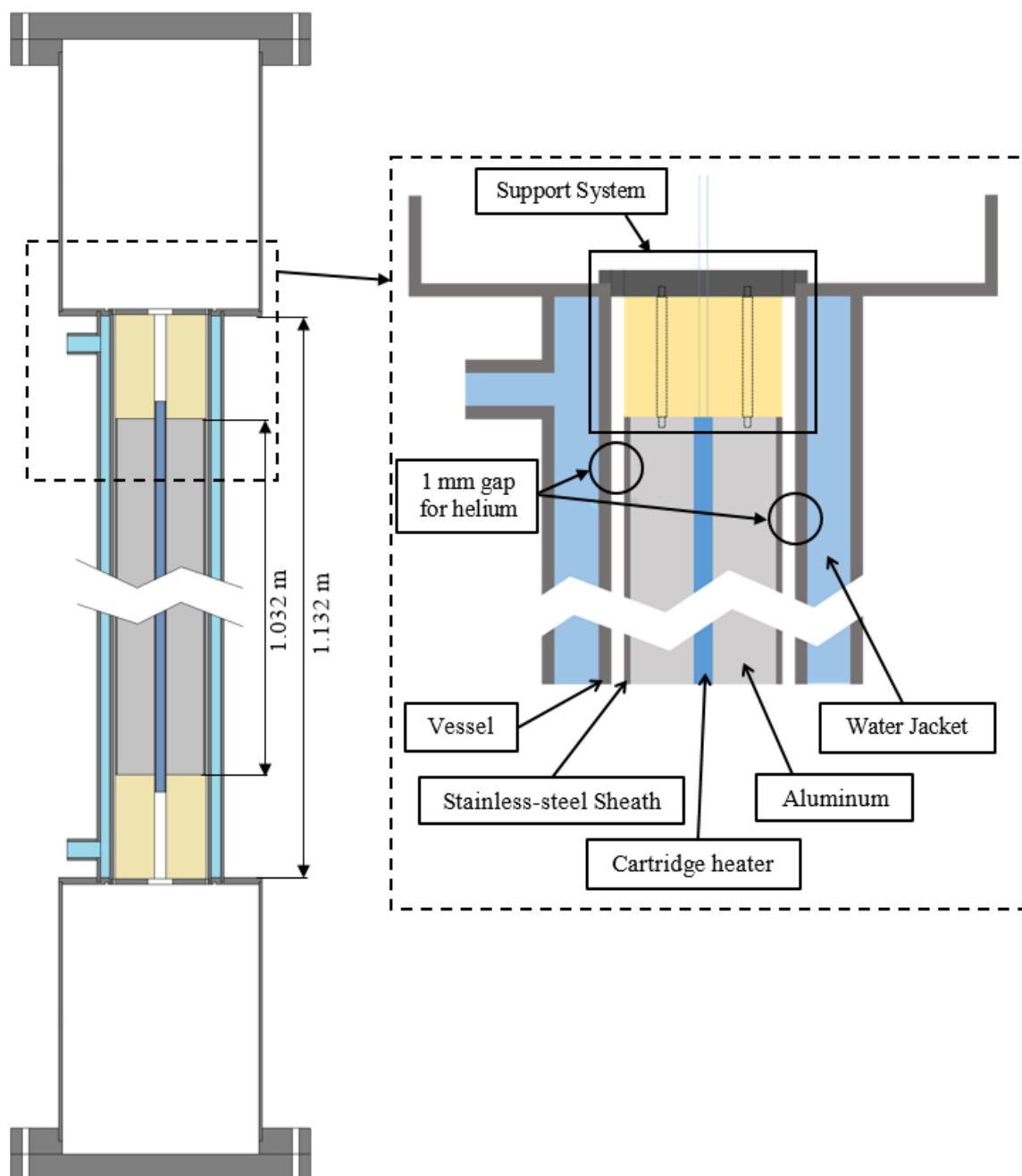
Figure 3.1. Cross-sectional view of the entire experimental apparatus with detailed view (not to scale) of the inner cylinder assembly and support system.

- Reduce the heat losses from the cylinders' end. The theoretical expression that is used to obtain the temperature jump and thermal accommodation coefficients assumes that heat is transferred only in the radial direction (no heat loss from the ends).

3.1.1. Overall system description

Figure 3.1 shows a cross-sectional view of the experimental apparatus. It consists of three main parts, the inner cylinder assembly, the pressure vessel along with the water jacket, and the support system. Each of these parts are described in detail in the following sections. The most important section of the experimental apparatus is the 1 mm annular gap that is maintained along a length of 1.037 m between the pressure vessel inner wall and outer wall of the inner cylinder assembly, which is held in place by support system with insulation at each end. This gap is clearly shown in the 'not to scale' detailed view that focuses on the end of the inner cylinder assembly, see Fig. 3.1. All dimensions for each of the three main parts are listed in Table 3.1, while all equipment needed for the experiment to function, along with their specifications, are listed in Table 3.2 for reference.

Table 3.1. Dimensions for main components in the three main parts of experiment.

Component	Dimensions [cm]		
	Outer diameter	Inner diameter	Length
Water Jacket	6.350 ± 0.003	6.02 ± 0.02	-
Vessel	5.071 ± 0.003	4.75 ± 0.02	147.29 ± 0.01
Stainless-steel Sheath	4.548 ± 0.02	4.45 ± 0.02	103.729 ± 0.003
Aluminum Cylinder	4.448 ± 0.003	1.27 ± 0.02	103.729 ± 0.003
Heating Cartridge	1.240 ± 0.003	-	105.410 ± 0. 003
Insulation	4.548 ± 0.003	-	4.272 ± 0.003
Ceramic Pin	0.635 ± 0.003	-	5.415 ± 0.003
Stainless-steel plug	4.448 ± 0.003	-	0.828 ± 0.003

Table 3.2. Description, quantity, and specifications of equipment used for experiment.

Equipment Name	Qty	Range	Uncertainty
Agilent 34970A Data Acquisition	1	N/A	1.0°C
Agilent 34970A Module, 20 Channel Multiplexer	2	N/A	1.5°C
Agilent N5770A Power Supply	1	150V, 10A, 1500W	0.125V to 0.20V
MKS Baratron Absolute Capacitance Manometer 626C	1	0.1 – 1000 Torr	0.25% for 1 to 1000 Torr, 0.50% for < 1 Torr
36 AWG K-Type Glass Braid Insulated SLE TC Wire	100 [ft]	N/A	0.5°C
Pfiffer HiCube 80 Vacuum Pump	1	<7.5x10^{-8} Torr	N/A
Lytron Recirculating Chiller	1	5°C - 35°C	± 0.5°C
NT12800 High Watt Cartridge Heater	1	120V, 1000W	+5/-10%
Manual Bellows Sealed SS Inline Valve	1	1x10-10 Torr	Leak Rate: 2x10-9 st. cc/sec
Fujikin Diaphram Soft-Seal Valve	1	N/A	N/A
Swagelok Metering Valve	1	N/A	N/A
Dry Helim UHP 99.999%	300C	N/A	N/A

3.1.2. Inner cylinder assembly

It consists of an electrical heating cartridge centered inside a thick walled aluminum cylinder with highly-conductive epoxy. Twelve thermocouples, grouped into three sections (top, center, and bottom), were strategically placed inside precision grooved channels machined on the outer surface of the aluminum cylinder and secured with highly thermal conductive cement so that any potential air gaps are minimized. The temperature induced interference fit process was used to insert the aluminum cylinder inside a 304 stainless-steel-sheath, which constitutes the outer piece of the inner cylinder assembly. This process was used to ensure an intimate contact between the outer aluminum surface and inner stainless-steel-sheath surface.

Figure 3.2 shows pictures of the inner cylinder assembly's top end (Fig. 3.2a) and bottom end (Fig. 3.2b), with the centered heating cartridge, aluminum cylinder and stainless-steel sheath along with the thermocouples and thermocouples channels. The aluminum cylinder

has a thick wall to allow uniform temperature profile on the outer surface of the inner cylinder assembly.
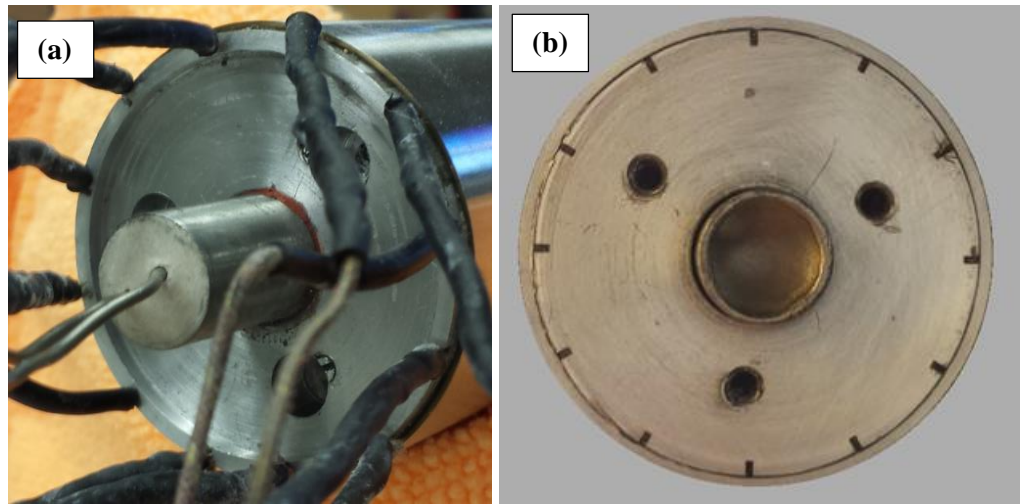
Figure. 3.2. Pictures of the inner cylinder assembly. (a) Top end showing the thermocouples, (b) bottom end showing the 1 mm thick stainless steel sheath.

To construction the inner cylinder assembly a stock round of aluminum 6061 was precision drilled and honed to ensure that the concentricity between the inner and outer diameters was maintained along its length. Next, the groove channels were machined and the thermocouples were secured inside them with cement, being careful not to contaminate the surface with excess cement. Once dry, the aluminum cylinder with the thermocouples was placed into a cryogenic environment of -150°C while a stainless steel cylinder (sheath) was placed into a large furnace at 427 °C. With the two cylinders at extreme temperatures the shrink fit was completed. Once cooled, the stainless steel sheath was machined down to 1 mm thickness. The final step was securing the heating cartridge into the center hole of the aluminum cylinder. Ensuring that only the heated portion of the cartridge was inside the aluminum cylinder. The cartridge was then secured with a high temperature compound for cylindrical metallic components (Loctite 7088) that would fill the 0.3mm gap between the aluminum and the outer surface of the heating cartridge.

3.1.3. Pressure vessel and water jacket system

Following similar pattern as for the inner cylinder assembly, twelve thermocouples are placed inside small grooves on the outer surface of the pressure vessel, made of 304 stainless steel, to provide a complete temperature profile. The temperature of the pressure vessel is controlled using an external water jacket. The thermocouples were secured inside the grooves with epoxy and aluminum straps to ensure their ability to withstand the turbulence of the water flow (see Fig. 3.3a). Figure 3.3b shows a picture of the water jacket that surrounds the pressure vessel. It shows two ports for the input and output of water from and to the chiller, respectively, and the instrumentation port for the thermocouple wires.

To construct the pressure vessel and water jacket, first grooves were machined into the side wall of the pressure vessel to allow for placement of the twelve thermocouples. The thermocouples were then secured into the grooves with epoxy and aluminum shim around the junction (see Fig.3.3a). The pressure vessel, with thermocouples, was then carefully placed inside a larger stainless-steel-jacket tube with the ports for water and thermocouple wires, aligned, and welded into place and the thermocouple wires carefully pulled through their port. The larger sections at each end of the pressure vessel and water jacket were needed to allow for ease of assembly.

3.1.4. Support system

The main functionalities of the support system is to hold the inner cylinder assembly centered inside the pressure vessel, and maintain a constant gap of 1 mm between the two. Another functionality is to minimize the heat losses from the inner cylinder assembly ends. The support system consists of three parts; the stainless steel plug, the insulation, and the ceramic pins. To ensure that the support system will fulfill its functions and allow for easy assembling, an iterative design process of the key components was accomplished. Figure 3.4 shows a picture of these components.
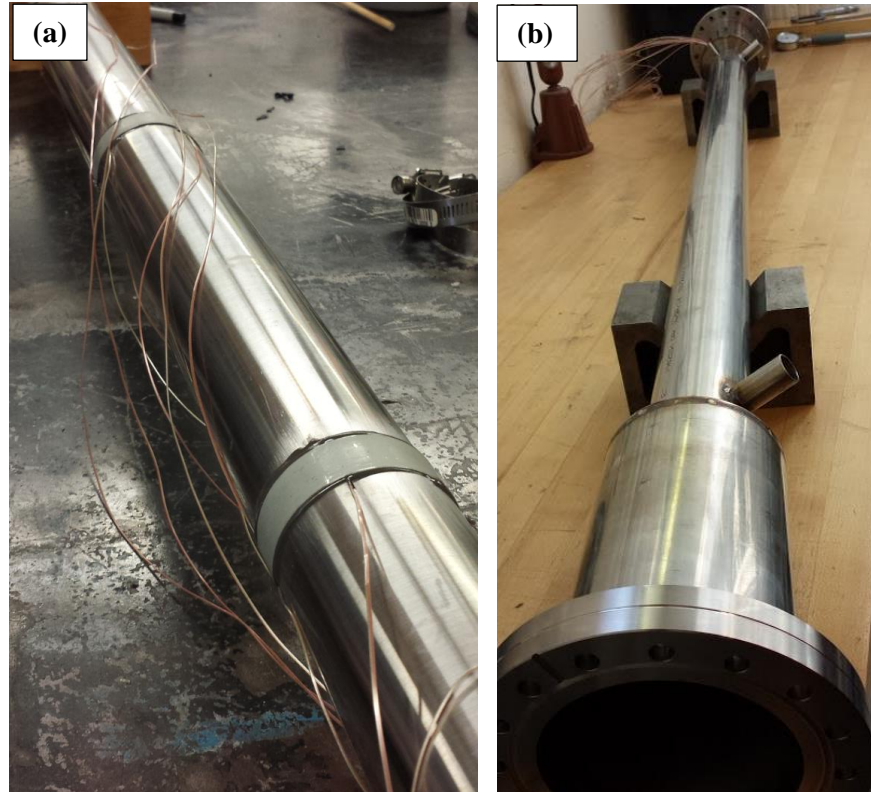
Figure 3.3. (a) Pressure vessel with thermocouples placed on the outer surface and secured with aluminum straps. (b) Water jacket that surrounds the pressure vessel shown with the thermocouples and water inlet and outlet ports.

The support plug (see Fig. 3.5.a) consist of 304 stainless steel cylinder that is 0.878 cm thick. The center hole is used to push through the power wires. The twelve holes drilled at the periphery of the plugs allow the thermocouple wires coming out of the inner cylinder assembly to pass through. The six holes that are patterned around the center hole are for the placement of the ceramic pins, which are used to align the insulation and support plug with the inner cylinder assembly, with only three pins used. The three tabs on the outside of the plug allow it to be secured to the pressure vessel while also ensuring that the inner cylinder is held concentric to the pressure vessel with 1 mm gap between them.

Figure 3.4. Picture of the support system. (a) Stainless steel plug, (b1) Bottom end alumina

insulation, (b2) Top end alumina insulation and (c) ceramic pins.

Figure 3.5. Different parts of the support system assembled together along with the inner

cylinder assembly.

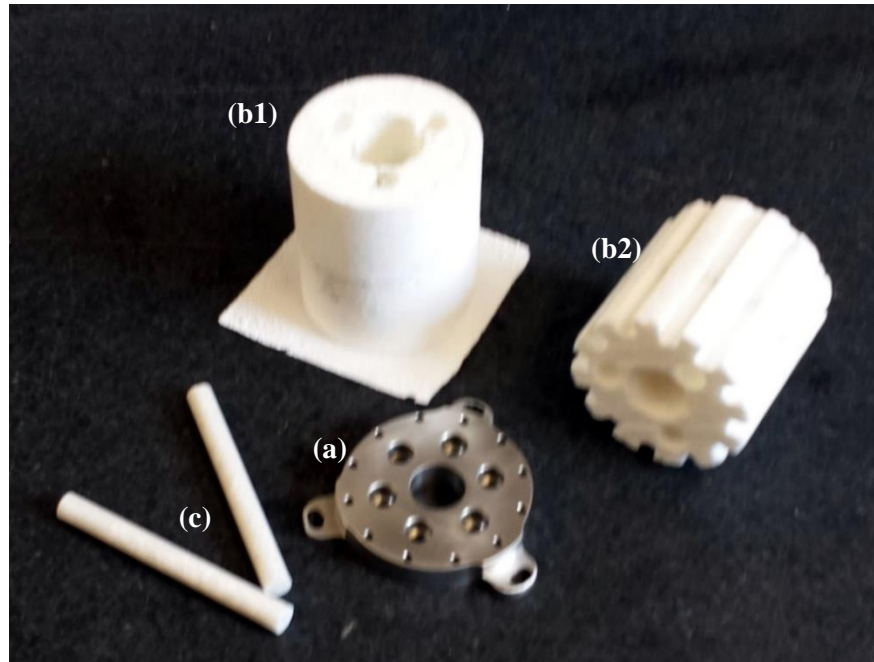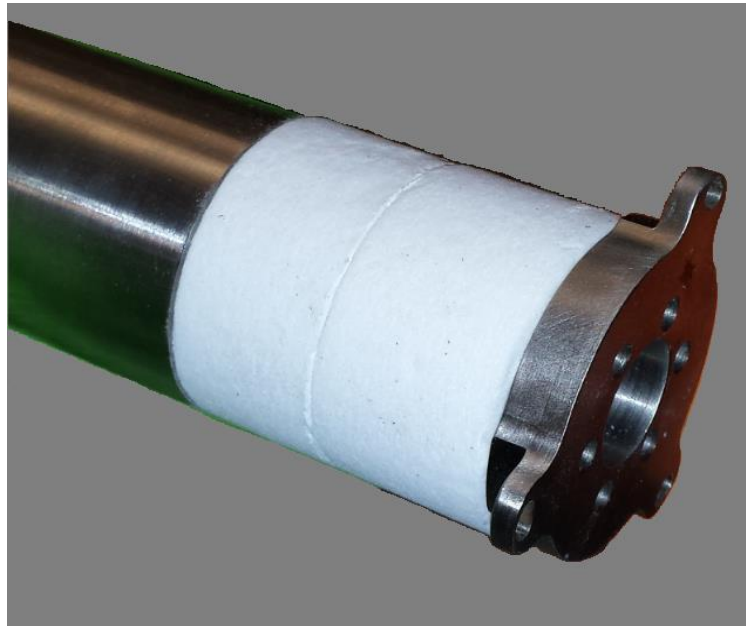Low thermal conductivity ($\kappa \approx 0.06$ W/mK) alumina insulation material, with a thickness of 5 cm, is placed on both ends of the inner cylinder system. The insulation is used to minimize the heat losses from the inner cylinder assembly ends and also to serve as a support for the inner cylinder to rest on. Three holes are drilled around the center hole for the ceramic pins. The insulation used on the thermocouple end of the inner cylinder assembly (see Fig. 3.4b2) has grooves that are machined on the outer surface to allow for the placement of the thermocouple wires.

Figure 3.5 demonstrates how the pins (Fig. 3.4c) help to align and to hold the insulation and the stainless steel support to the inner cylinder assembly.

3.1.5. Assembling of the experiment

A careful procedure to assemble the inner cylinder assembly with the pressure vessel was meticulously followed. The assembling was realized in horizontal position for convenience. The inner and outer walls of the pressure vessel and inner cylinder assembly, respectively, have to be protected against scratching or damaged. Also the 1 mm gap between the two must be maintained. To ensure that the functional walls of the experiment are not scratched or damaged, plastic spacers made out of Acetal Homopolymer, were employed. These spacers were added to the top and bottom of the inner cylinder assembly and pressure vessel, and served as guidance during the insertion of the inner cylinder assembly into the pressure vessel. Once the inner cylinder assembly was placed inside the pressure vessel, the bottom insulation, ceramic pins, and support plug were inserted and secured using three screws, see Fig. 3.6a. It should be noted that the plastic spacers were maintained in place during all the assembling steps. The experiment was then oriented vertically and the top insulation, ceramic pins, and support plug was inserted and secured, see Fig. 3.6b.
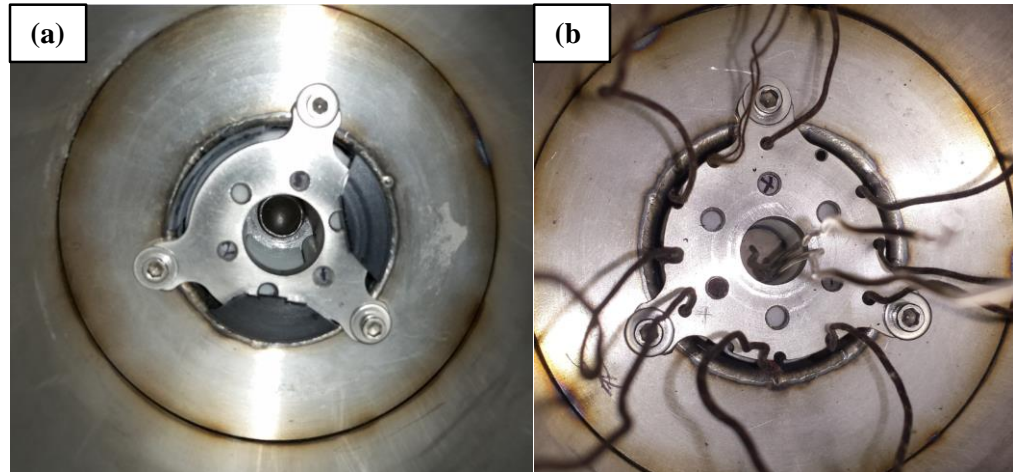
Figure 3.6. Bottom (a) and top (b) insulation, ceramic pins, and support plug secured in place with screws.

The next procedure in the assembly process was to make the vacuum side instrumentation and power connections to the feedthrough.

3.1.6. Power and thermocouples' connections

A Multi-Pin ConFlat (CF) vacuum flange feedthrough, configured for type K thermocouples and power connections, was used to take the thermocouple and power wires from the vacuum side to the air side of the experiment. Reference single ended wiring was used for the thermocouples and direct connections for the power wires. Soldering was used to connect the thermocouple and power wires to the feedthrough. A high temperature heat shrink tubing was used to ensure that all the wires were independently isolated from each other, with the final result of this step shown in Fig. 3.7.

The CF flange was then sealed and bolted to the experimental apparatus, and the thermocouple and power wires from the air side of the feedthrough were connected to the Agilent 34970A Data Acquisition/Switch Unit (DAQ) and Agilent N5770A power supplier, respectively.

Figure 3.7. Thermocouple and power wires connected to vacuum side of feedthrough.

3.1.7. Vacuum tree assembly

The vacuum tree consists of a stainless steel tube attached to a CF flange. The following components of the vacuum tree are attached to the stainless steel tube:

- MKS Baratron Absolute Capacitance Manometer 626C.

- Diaphragm Soft-Seal valve and Swagelok metering valve that allows for a very accurate control of helium inlet to the experiment.

- Manual bellows sealed SS Inline valve that isolates the experiment from the vacuum pump.

- Pfiffer HiCube 80 vacuum pump.

Figure 3.8 shows the vacuum tree with each component labeled, connected to the experiment.
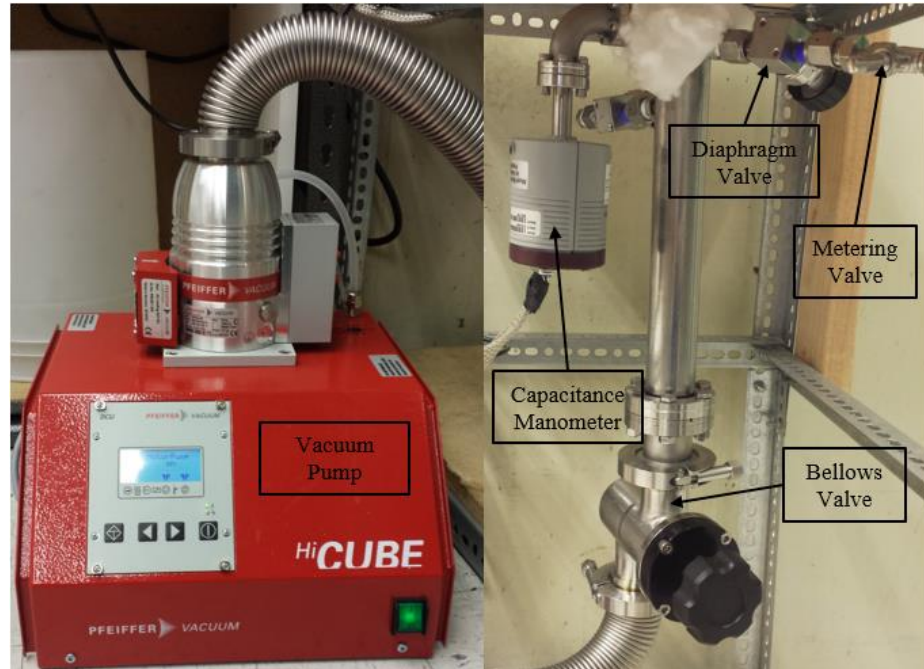
Figure 3.8. Vacuum tree assembly.

3.1.8. Preliminary testing

The following tests were performed on the experimental setup:

- All inner cylinder assembly and water jacket thermocouples were tested to ensure their full functionality before and after construction or assembling of each components. As a result, all twelve water jacket thermocouples were fully functional, however, only eight of the inner assembly thermocouples were fully functional after the final assembling.

- The voltage and current supplied to the heating cartridge was confirmed with a digital multimeter at both the power supply connections and air side of the feedthrough.

- The pressure vessel was evacuated and backfilled numerous times to ensure that the only gas present in the system is helium.

- Leak and outgassing tests were performed to find and eliminate any possible leaks and to know the outgassing rate, which can affect the pressure reading. The tests using the

leak detector showed that there was no leak, however the outgassing rate was important.

To check and decrease the outgassing rate the standard '*rate of rise*' method was employed. The pressure in the experiment was set to its possible lower value (10^{-2} Pa) using the vacuum pump and the temperature was raised to a constant value of 160°C for several days. Decreasing the pressure and baking the experiment enables adsorbed gas/vapor to be evacuated, so that outgassing rate to be decreased. The vacuum pump was then isolated and the rise of pressure was monitored. If the pressure rises significantly, that means that the system still outgassing. This method was repeated several times until the pressure gauge was not sensitive to this effects.

Other tests were conducted to check the time needed for the experiment to attain the steady state and also that there is a measureable temperature difference between the inner cylinder assembly and the pressure vessel walls, even at higher pressures. All the above tests showed that the experiment is suitable for the observation of the rarefaction effect and measurements of the temperature jump and thermal accommodation coefficient.

3.2 Validation of the experimental design

A geometrically accurate three-dimensional model of the experimental apparatus was created and meshed using ANSYS/Fluent CFD commercial code. Simulations that include conduction and radiation heat transfer, and temperature-jump at the interface between solid surfaces and gas were performed. The outer surface of the vessel was maintained at a constant temperature of 27.85°C and the pressure in the gap was varied from atmospheric pressure to $P = 200$ Pa. This range of pressures covers both continuum and slip regimes. Three values of the thermal accommodation coefficient, $\alpha = 1$, 0.4, and 0.2, and constant heat generation rates within the cartridge heater (Q=100W, 150W, and 200W) were considered for all the simulations. The

expression of temperature jump coefficient proposed by Lin and Willis (see Eq. 2.6) is implemented in ANSYS/Fluent simulations.

These simulations are used to check the ability of the apparatus to measure the effect of rarefaction. The effect of heat losses from the cylinder's ends on the measurement of the thermal accommodation coefficient is also investigated. The assumptions of constant temperature and heat flux profiles along the z-axis is verified.

Figure 3.9 shows a typical cross-section-temperature-contour for all of the simulated cases considered. The maximum temperature is located at the center of the inner cylinder assembly with nearly uniform temperature through the aluminum cylinder and stainless steel sheath surrounding the aluminum cylinder. A steep decrease in temperature is observed across the helium gas gap.
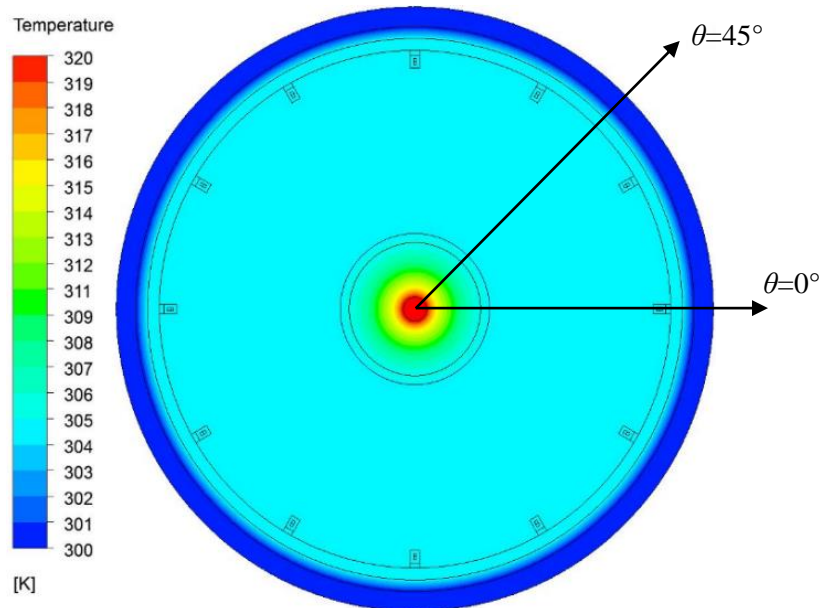

Figure 3.9. Typical temperature contour for all simulated cases.

Figure 3.10 shows the profiles of the temperature along the r-axes shown in Fig. 3.9 for $\theta=0°$ (across a thermocouple) and $\theta=45°$, for $Q=150W$, and a continuum condition ($P=1$ atm). The temperature profiles along the two axes are very similar and the only difference is obtained at

the thermocouples location, where the thermocouples experience slightly lower temperature difference on the order of 0.1°C. Even when varying the heat generation rate Q from 100W to 200W the temperature difference across the thermocouple remains small (less than 0.15°C).
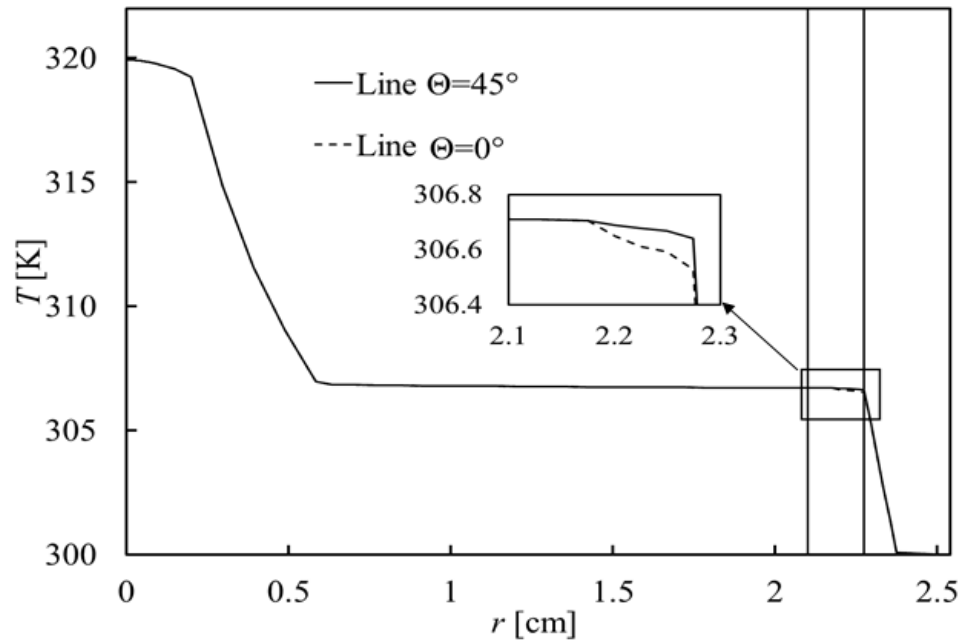
Figure 3.10. Temperature profile along the r-axis shown in Fig. 3.9 for atmospheric pressure (Continuum Model).

In Fig. 3.11, the effect of rarefaction on the increase in temperature, compared to the continuum model, is shown. The rarefaction simulation are performed for P=300 Pa and α=1, 0.4, and 0.2. From Fig. 3.11 it can be seen clearly that the rarefaction model predicts higher temperature in comparison to the continuum model, which is due to the temperature-jump at the interface between solid surfaces and gas. This temperature increases as the thermal accommodation coefficient decreases.

Temperature profiles along the cylinder axis (z-axis) are shown in Fig. 3.12 for the outer surfaces of the stainless steel sheath and thermocouple region. These profiles are obtained using the continuum model. A nearly uniform temperature along the stainless steel sheath surface is

obtained. The maximum variation of temperature along this surface is less than 0.1℃ with the value obtained at the mid-plane.
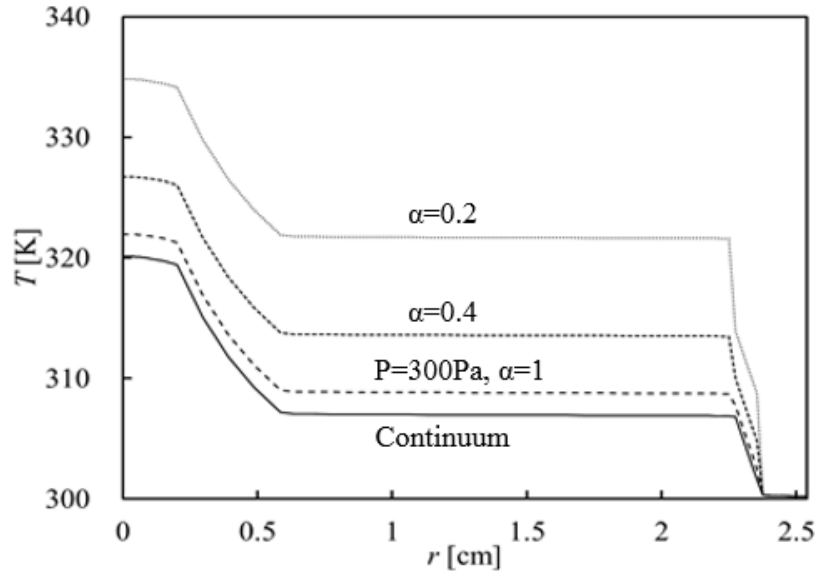
Figure 3.11. Comparison between continuum (*P*=1 atm) and rarefaction model (*P*=300 Pa) for different values of the thermal accommodation coefficient.

Axial heat flux profiles along the side surfaces of the stainless steel sheath and vessel are shown in Fig. 3.13. It is clear from this figure that the heat flux leaving the outer surface of the stainless steel sheath and delivered to the inner surface of the vessel, which are in contact with helium, are nearly identical and uniform along the axial axis direction. The maximum variation of the heat flux along the axial axis is less than 1%.

The uniformity of the temperature and heat flux leaving the surfaces in contact with helium, shown in Figs. 3.12 and 3.13 confirms the validity of the actual experimental design to be used for the calculation of the value of the temperature jump coefficient and thermal accommodation coefficient.
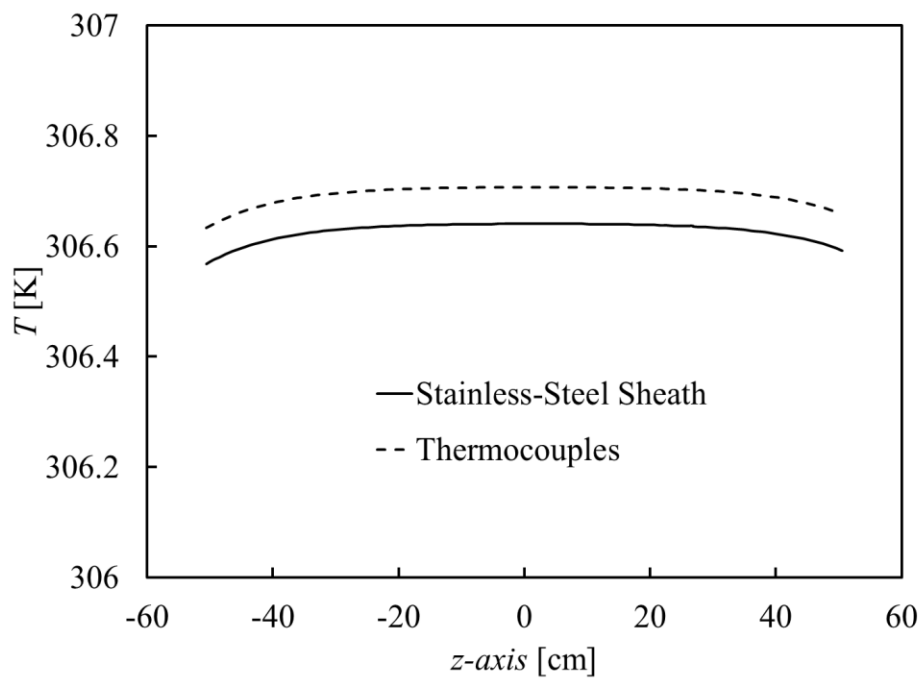
Figure 3.12. Axial temperature profiles for the outer surface of the stainless steel sheath and the thermocouple region.

Figure 3.13. Heat along the vessel inner surface and outer surface of the stainless steel sheath.

Heat losses from both ends of the inner cylinder assembly are minimized by choosing a cylinder with small aspect ratio R_i/L=0.02, where R_i and L are the radius and length of the inner cylinders system, respectively, and by placing low thermal conductivity alumina insulation material (κ=0.06 W/m.K) on both ends of the inner cylinders system. Table 3.3 shows the percentage of the estimated heat leaving from the side and ends surface of the inner cylinders system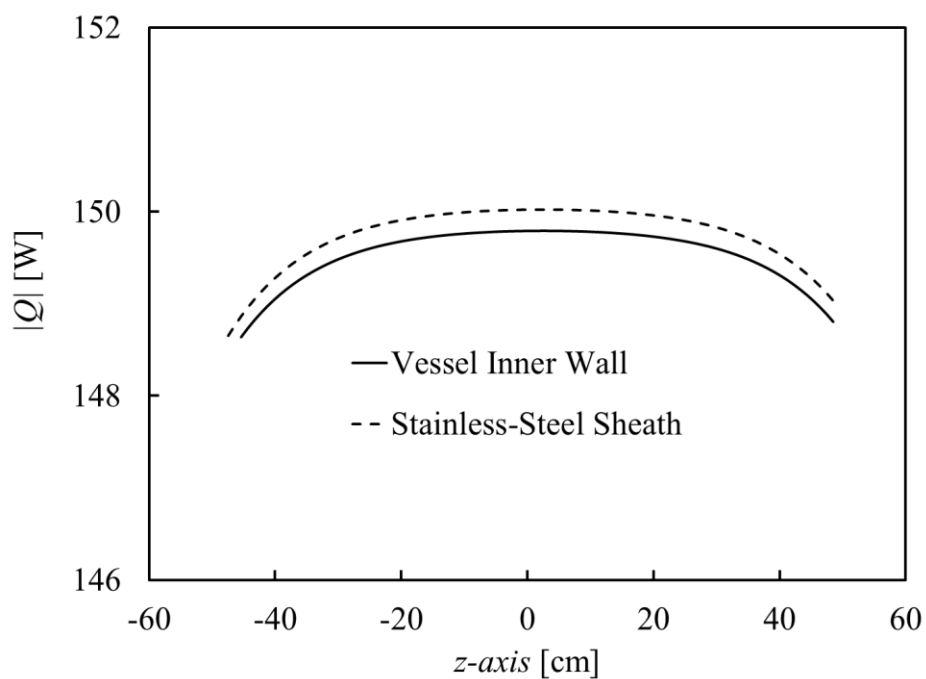 for continuum and rarefied models with three different values of thermal accommodation coefficient. Table 3.3 shows that the heat loss from both ends of the inner cylinder assembly is less than 1.2%.

Table 3.3. Percentage of heat loss from the side and ends of the inner cylinder system.

	α	Percentage of wall heat flux [%]	
		Side-Walls	End-Walls
Continuum	-	99.66	0.34
$P = 300$ Pa	1	99.13	0.87
	0.4	98.97	1.03
	0.2	98.88	1.12

The predicted temperature difference between the stainless steel sheath and the pressure vessel inner wall as a function of pressure is shown in Fig. 3.14, for different values of the thermal accommodation coefficient from the two dimensional model. By comparing the measured temperature difference and predicted temperature difference found in the simulations, the temperature jump and/or thermal accommodation coefficient can be determined.

3.3. Extraction of α and uncertainty calculation

Replacing the expression of the Knudsen number (2.3), the mean free path (2.1), and temperature jump (2.6) in equation (2.8), the temperature difference ΔT can be written as function of the inverse of the pressure as

$$T_{in} - T_{out} = \frac{Q_r}{2\pi L\kappa} \mu \zeta_T \left(\frac{1}{R_A} + \frac{1}{R_B} \right) \sqrt{2\frac{k_B}{m}T_{out}} \frac{1}{P} + \frac{Q_r}{2\pi L\kappa} \ln\frac{R_{out}}{R_{in}} \,. \tag{3.1}$$
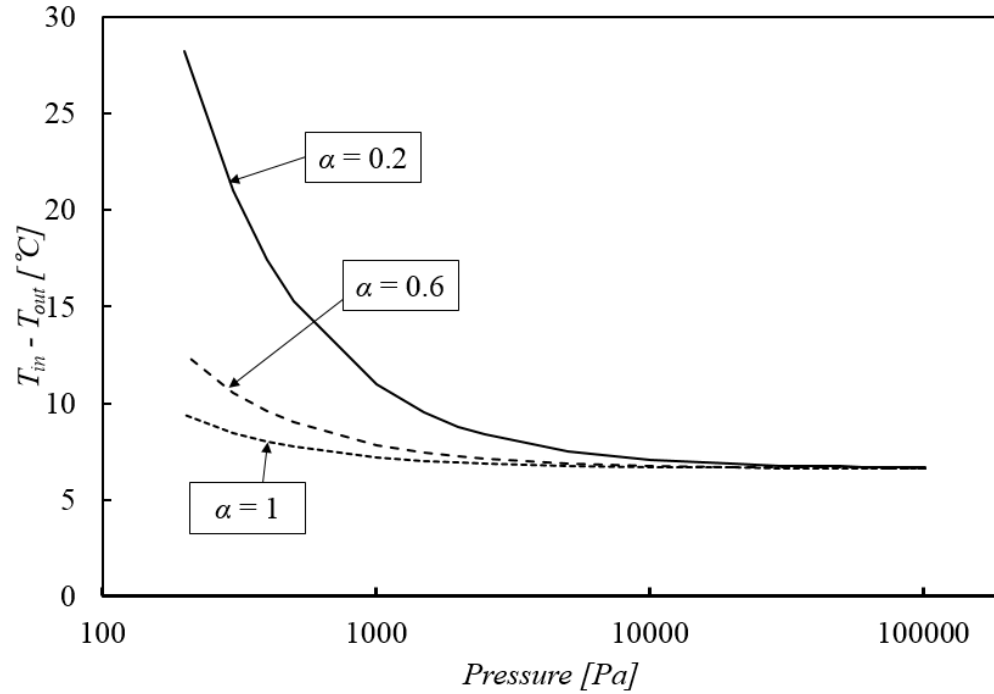
Figure 3.14. Temperature difference for range of pressures and $Q=150W$ for different values

of α.

It is clear from this expression that the temperature difference T_{in}-T_{out} is linear function of the

inverse of the pressure. The expression (3.1) will be used for comparison with experimental

data to extract the value of the thermal accommodation coefficient α. The experimental

measurements of the temperature difference T_{in}-T_{out} will be carried out for a constant value of

the heat flux Q and the different values of the pressure P. The measured data of T_{in}-T_{out} as

function of the inverse of the pressure will be plotted and fitted with first order polynomial

form using the least square method as

$$T_{in} - T_{out} = a\frac{1}{P} + b,$$ (3.2)

where a is the slop of the function. The slope a can be expressed as function of the thermal

accommodation coefficient as

$$a = \frac{Q_r}{2c_p \, L} \frac{\gamma}{\gamma + 1} \left(\frac{2 - \alpha}{\alpha} + 0.17 \right) \left(\frac{1}{R_A} + \frac{1}{R_B} \right) \sqrt{\frac{2}{\pi} \frac{k}{m} T_B} \, , \qquad (3.3)$$

Chapter IV
Results and Discussions

Measurements of temperature difference across rarefied helium enclosed between two coaxial cylinders are carried out over a range of pressures from 150 Pa to 101325 Pa (1 atm), which covers the continuum and slip regimes. The measurements were performed for three different heat generation rates Q=100W, 150W, and 200W. Recirculating cooled water through the water jacket by using the chiller has enabled the control of the pressure vessel outer surface temperature, so that T_{out}=26.5 ± 0.5 °C. The inner and outer temperatures of the inner cylinder assembly and pressure vessel, respectively, were measured using eight thermocouples placed on the periphery of the inner cylinder assembly and twelve thermocouples placed on the outer surface of the pressure vessel. The experimental results were collected over a period of three months, from June to August 2015. Prior to collecting the experimental data, extensive testing was performed to ensure that the experiment was robust and functioned properly along with the development of a standard procedure and methodology as to how the measured data would be collected.

4.1. Procedure and methodology

To ensure that the collection of the experimental data are repeatable and systematic errors are minimized, a methodology was developed and followed during each experimental run.

- First, the chiller is turned on and programmed to the temperature of 26.5 ± 0.5°C, then the internal heating cartridge is activated to allow the inner assembly thermocouples were allowed to reach steady state.

- Second, the pressure gauge is zeroed to 0 ± 0.05 mV, then the inline valve is closed to isolate the vacuum pump from the experiment.

- Third, helium is introduced to the system by, first, opening the diaphragm valve and then controlling the input of helium with the metering valve to reach the desired pressure setting and, finally, closing both metering and diaphragm valves.

- The Agilent 34970A DAQ is used in conjunction with LabView to collect the inner cylinder assembly (T_i) and pressure vessel (T_o) temperatures along with monitoring the ambient temperature and the helium pressure.

- After collecting the necessary data for the day, the power supply and chiller are both turned off and the vessel is put back to vacuum conditions.

4.2. Thermocouple's temperature as function of heat generation

Figure 4.1 shows the inner cylinder assembly and pressure vessel individual thermocouple's temperatures, T_{in} and T_{out}, respectively, as function of the heat generation rate, Q, for continuum conditions (atmospheric pressure). It can be seen from this figure that as heat generation increases, both inner, T_{in}, and outer, T_{out}, temperatures increase. However, the increase of the outer temperature (pressure vessel) is relatively small, less than 1°C. Also, it shows that for a given heat generation rate ($Q > 0$ W), the inner temperatures, T_{in}, at different axial locations (top, center, and bottom) are different. However, the outer temperatures, T_{out}, at different axial locations are almost the same, the differences are less than 1°C. This shows that the water jacket has fulfilled its function of keeping relatively uniform temperature along the axial axis of the pressure vessel, and also when the heat generation is varied. Figure 4.1 also shows that when $Q = 0$ W (cartridge heater turned off) there is a measureable difference between the inner, T_{in}, and outer, T_{out}, temperatures of 0.7°C. The inner temperatures are lower than the outer temperatures, which suggests a systematic measurement error.
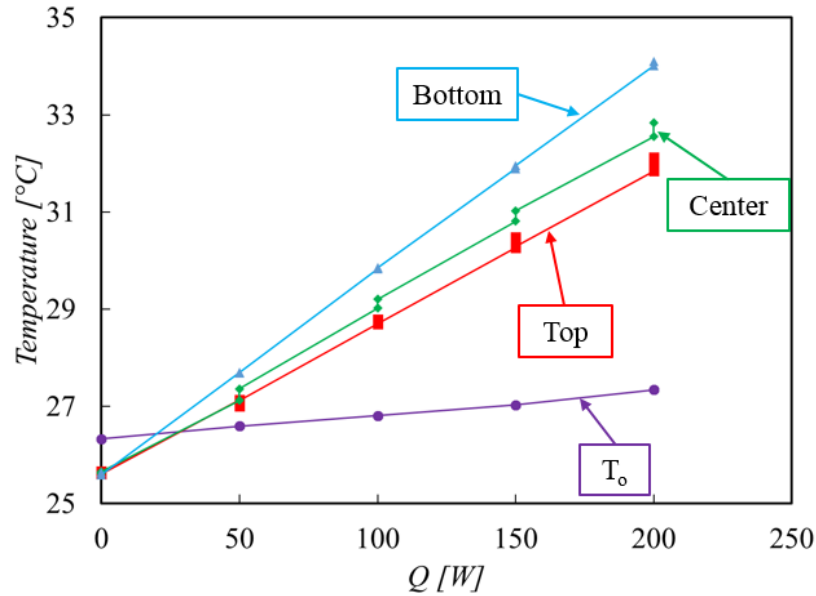
Figure 4.1. Inner cylinder assembly temperatures, T_{in}, and pressure vessel inner wall temperatures, T_{out}, for different heat generation rates, Q, at atmospheric pressure (continuum regime).

Simulations predicted (see Sec. 3.2) that the temperature along the axial axis of the inner cylinder assembly will be constant. However, from Fig. 4.1, it can be seen that the difference between the inner thermocouple's temperatures at different locations increase as the heat generation rate Q increases. The top thermocouples measure lower temperatures compared to the bottom ones, which may suggest that there is more heat loss from the top end of the inner cylinder assembly. This suggests some uncertainties that could be related to the design and geometry of the experiment. One possible uncertainty may be an incorrect estimation of the heat losses from the inner cylinder assembly ends (see Tab. 3.3). The thermocouple and power wires leaving the inner cylinder assembly from the top end may be conducting more heat than estimated from the simulations, and/or the insulation used at both ends of the inner cylinder assembly may not have as low of conductivity as specified by the vendor. Another possibility may be a shift of the inner cylinder assembly inside the pressure vessel, which can make the

inner cylinder assembly and the pressure vessel to not be concentric. The eccentricity will cause a non-uniformity of the heat flux along the radial direction of the inner cylinder assembly. More heat will leave the small space between the cylinders than the larger spaces. A break of the ceramic pins that hold the inner cylinder assembly concentric to the pressure vessel may cause this. A final possible uncertainty could be an error in the measurement of the diameter of the pressure vessel inner wall. Due to its length, the measurement of the inner diameter along the entire length was not possible, therefore, measurements were taken from each end as far as 15.24 cm inside, leaving a length of 116.81 cm, where the inner diameter could not be confirmed.

4.3. Comparison between the measured and simulated results

Figures 4.2 – 4.4 show a comparison of the experimentally measured average temperature difference between the stainless-steel-sheath inner wall, T_{in}, and the pressure vessel outer wall, T_{out}, with the simulated results, for different heat generation rates, Q=100W, 150W, and 200W, as a function of pressure. The simulation results were obtained for three different values of the thermal accommodation coefficient, $\alpha = 1$, 0.6, and 0.2. These figures show that the measured temperature difference, T_{in} - T_{out}, is almost constant in the continuum regime ($21820 < P < 101325$ Pa), however in the slip regime ($218.2 < P < 21820$ Pa), the temperature difference increases as the pressure decreases. As an example, for the case $Q = 100$ W and $P \approx 200$ Pa, the temperature difference is 10°C higher than it is at $P \approx 10^5$ Pa. This measureable difference is due to the rarefaction effect (decrease of pressure), which proves that our first objective, namely "to observe the rarefaction effect", was successfully accomplished.
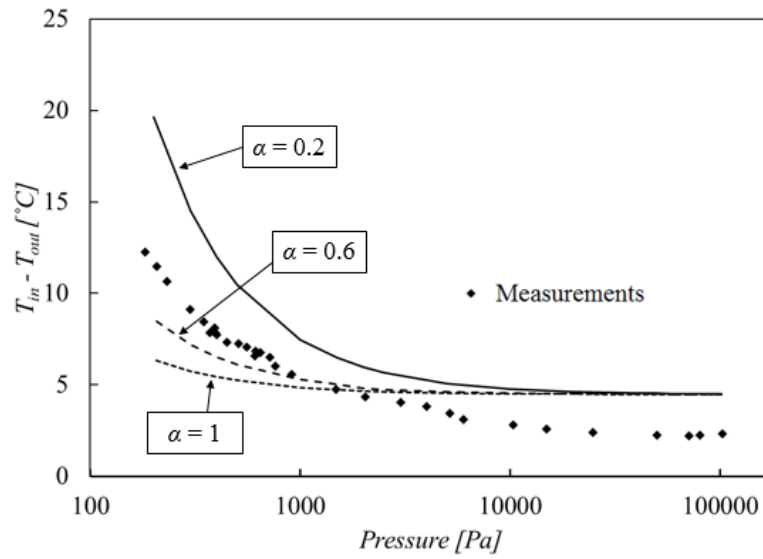
Figure 4.2. Measured results compared to simulated results for $Q=100W$ and different value

of the temperature jump coefficient.
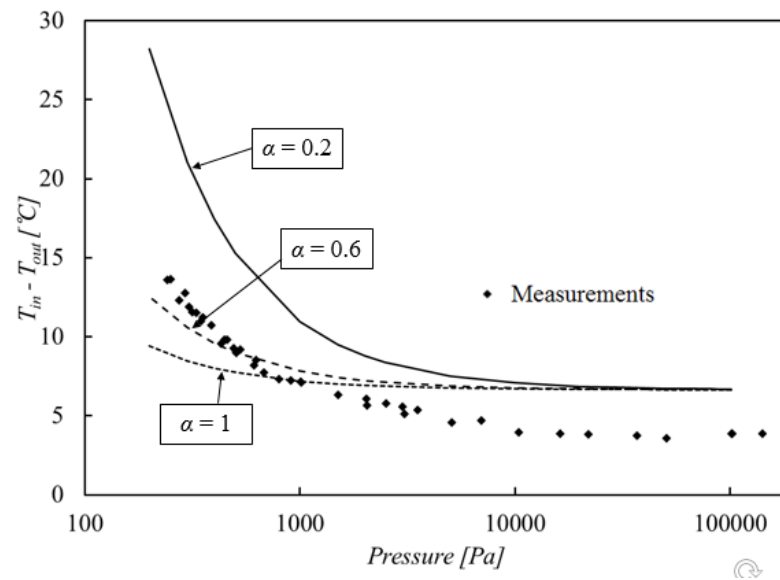

Figure 4.3. Measured results compared to simulated results for $Q=150W$ and different value
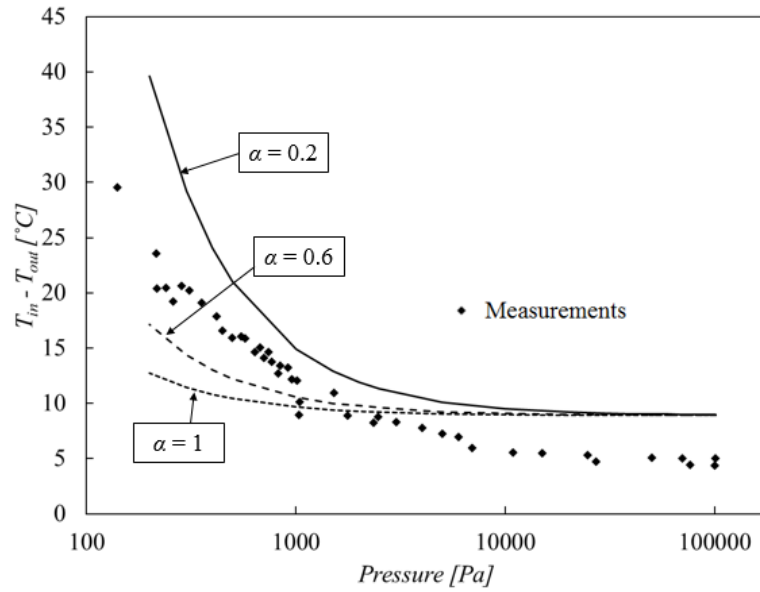
of the temperature jump coefficient.

Figure 4.4. Measured results compared to simulated results for Q=200W and different value of the temperature jump coefficient.

It can also be seen from Figs. 4.2 – 4.4 that the profiles of temperature difference as function of pressure obtained from measurements and simulations follow the same trend. However, at high pressures (continuum regime) there is a noticeably difference between the measured and the simulated results. The simulated results predict temperature differences at high pressures that are 4.5°C, 6.7°C, and 9.0°C for the heat generation rates Q=100W, 150W, and 200W respectively. However, the measured temperature differences are 2.3°C, 3.9°C, and 5.0°C, respectively, which shows a noticeable difference between the measured and simulated results of 2.2°C, 2.8°C, and 4.0°C, respectively. This difference increases with heat generation rate, which is expected since it was seen in Fig. 4.1 that there is an increasing measureable difference between the top, center, and bottom inner thermocouples temperatures as the heat generation rate increases. As explained in the previous section, a reason could be an incorrect estimation of the heat loss or wrong measurement of the pressure vessel inner diameter, or a shift of the inner cylinder assembly inside the pressure vessel. Also, this difference at continuum regime

should take into consideration the systematic error suggested in Fig. 4.1 at $Q = 0$ W. Two investigations were performed to determine the cause for this difference and are discussed in details in the next two sections.

4.4. Uncertainty on the pressure vessel inner diameter

To check if an error in the measurement of the pressure vessel inner wall diameter is the reason for the discrepancy between the measured and simulated results of the temperature difference between the inner cylinder assembly and the pressure vessel, an analytical calculation of the diameter of the pressure vessel inner wall that would cause the simulation to match the measurements of the temperature difference at atmospheric pressure for the top and bottom thermocouples was performed. The calculations yielded to the following diameters, ID_{Top}=4.58 cm and ID_{Bottom}=4.59 cm, for the top and bottom thermocouples, respectively, which are 0.17 and 0.16 cm smaller than the nominal measured diameter ID=4.75 cm, respectively. These diameters were then utilized in ANSYS/Fluent to calculate the temperature difference T_{in} - T_{out} as a function of pressure for each of the heat generation rates, Q=100W, 150W, and 200W and for α=0.4.

Figures 4.5 – 4.7 show the individual top and bottom thermocouple's temperature differences along with the simulation results for the two pressure vessel inner diameters ID_{Top}=4.58 cm and ID_{Bottom}=4.59 cm as function of the pressure. At higher pressures, $P > 10000$ Pa, there is a good agreement between the measured and simulated results for all the heat generation rates Q. As pressure decreases, $P < 10000$ Pa, the measured temperature differences start to deviate from the simulated results. The measured temperature differences are higher than the simulated ones and the difference between them increase as the heat generation increases. It should be noted that the calculated diameters ID_{Top} and ID_{Bottom} are beyond the range of uncertainty specified by the vendor, $\pm$ 0.02. This suggests that the possible uncertainty being an error in the measurement of the diameter of the pressure vessel inner wall is not a strong contributor to the

Figure 4.5. Comparison between the temperature differences for the top and bottom thermocouples obtained experimentally and numerically using the inner diameters ID_{Top}=4.58 cm and ID_{Bottom}=4.59 cm, for Q=100W and α=0.4.

Figure 4.6. Comparison between the temperature differences for the top and bottom thermocouples obtained experimentally and numerically using the inner diameters ID_{Top}=4.58 cm and ID_{Bottom}=4.59 cm, for Q=150W and α=0.4.
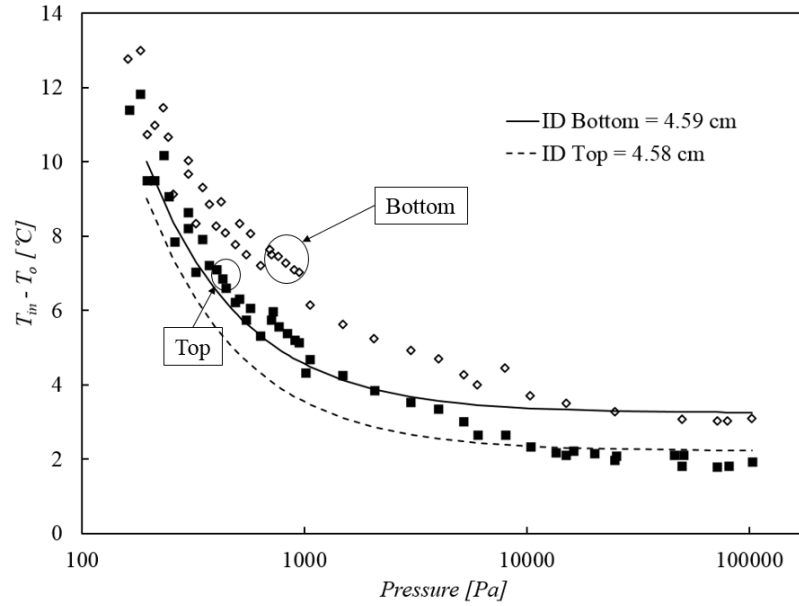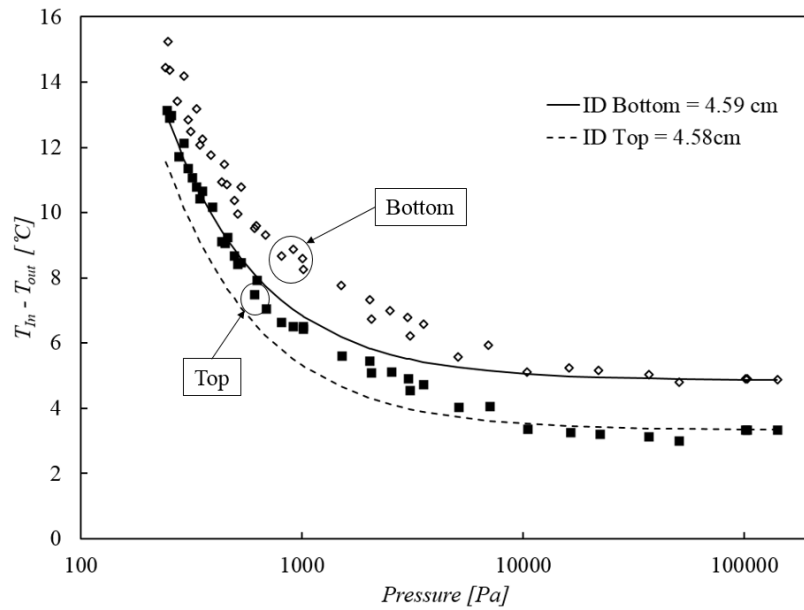
Figure 4.7. Comparison between the temperature differences for the top and bottom thermocouples obtained experimentally and numerically using the inner diameters ID_{Top}=4.58 cm and ID_{Bottom}=4.59 cm, for Q=200W and α=0.4.

differences seen between the measured and simulated results in Figs. 4.2 – 4.4. Other possibilities should be investigated.

4.5. Uncertainty on the inner cylinder eccentricty

For the second case we consider the inner cylinder assembly being shifted inside the pressure vessel, ANSYS/Fluent models were constructed with the inner cylinder assembly shifted in the radial direction to one side to create an eccentric model. This was done for different percentages of offsets ($x/(R_{out} - R_{in})\times100$) ranging from 20% to 95%, where x is the value of the offset in centimeter. It was found that the 70% and 90% offsets give the closet temperature differences to the bottom and top measured temperature differences in the continuum regime, respectively, for all heat generation rates, so these values were retained.
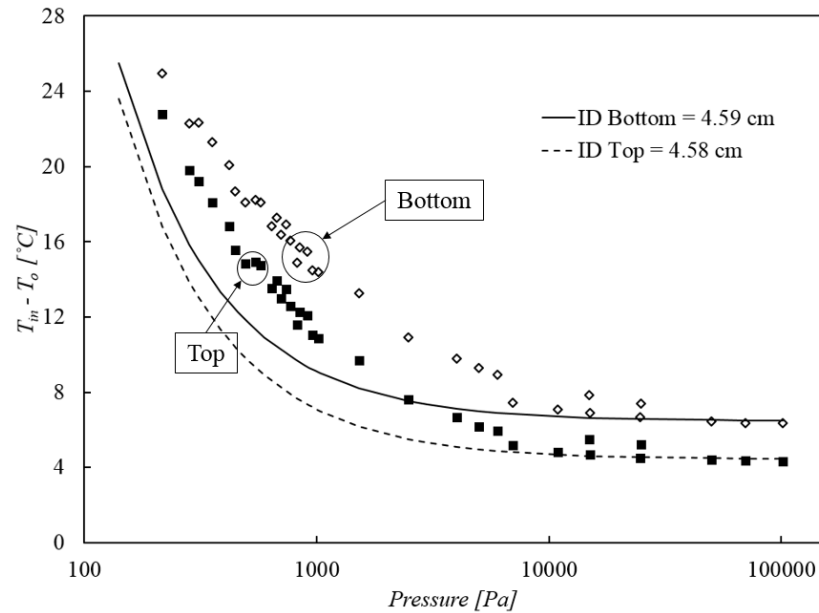
Figure 4.8. Comparison between the temperature differences for the top and bottom

thermocouples obtained experimentally and numerically using offsets of 70% and 90% for

the inner cylinder assembly, for Q=100W and α=0.4.

Figure 4.9. Comparison between the temperature differences for the top and bottom

thermocouples obtained experimentally and numerically using offsets of 70% and 90% for

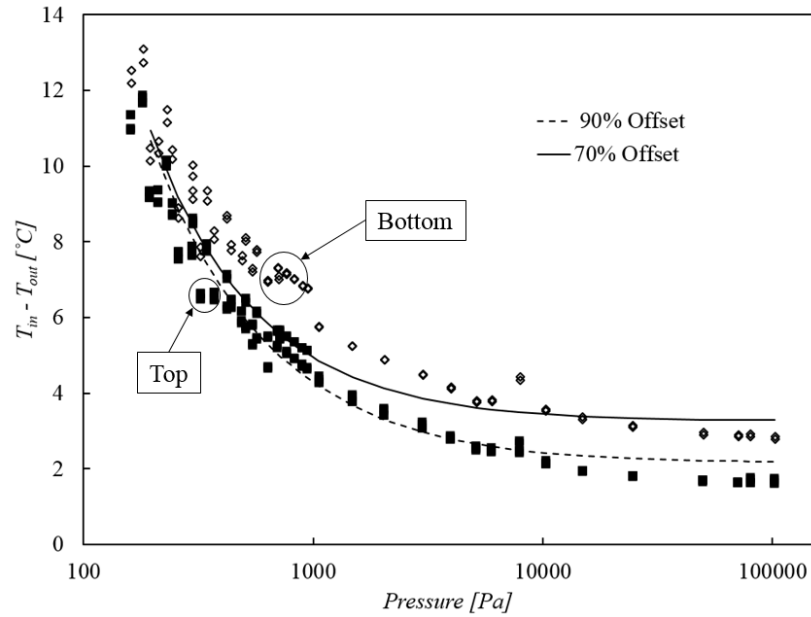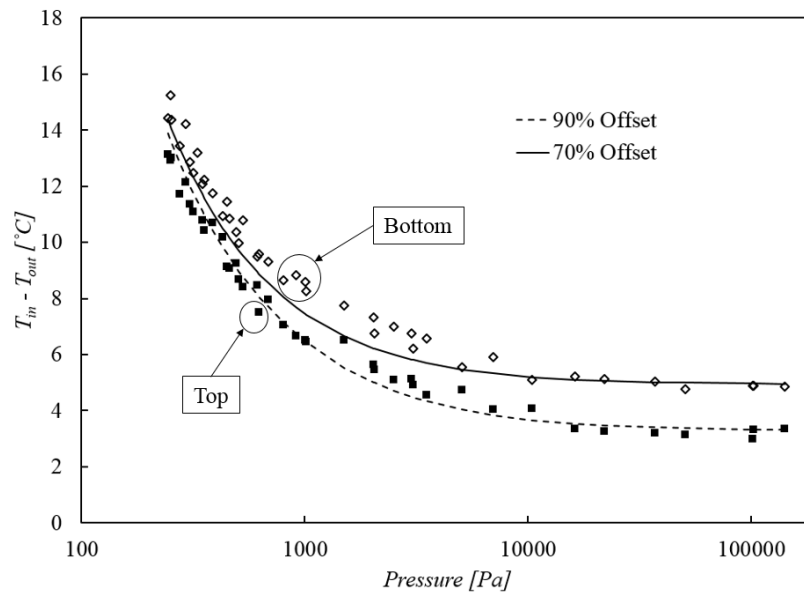the inner cylinder assembly, for Q=150W and α=0.4.
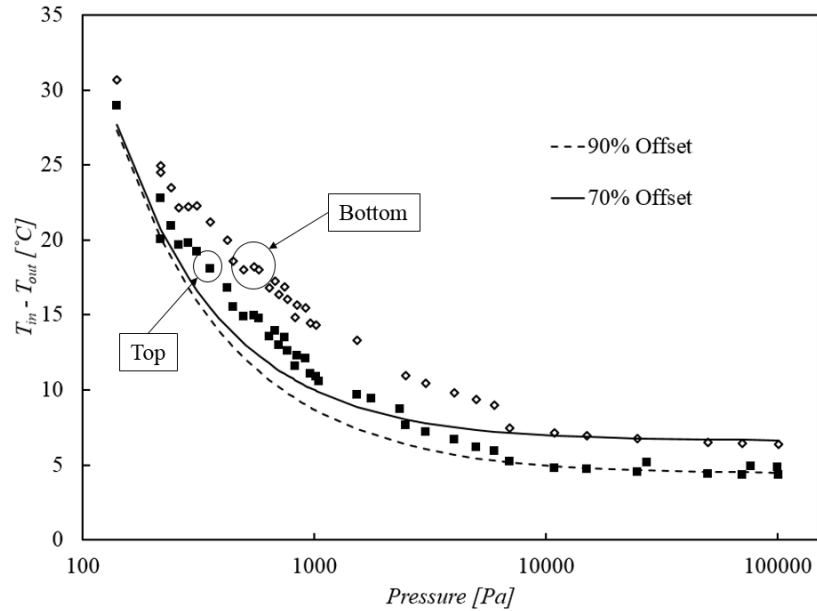
Figure 4.10. Comparison between the temperature differences for the top and bottom

thermocouples obtained experimentally and numerically using offsets of 70% and 90% for

the inner cylinder assembly, for Q=200W and α=0.4.

Figures 4.8 – 4.10 shows a comparison between the temperature differences for the top and

bottom thermocouples obtained experimentally and numerically using ANSYS/Fluent for the

offsets of 70% and 90%, corresponding to the bottom and top thermocouples, respectively, for

the heat generation rates, Q= 100 W, 150 W, and 200 W and thermal accommodation

coefficient α=0.4. It can be seen from these figures that at the high pressure ($P \geq 10000$) the

simulated results for 70% and 90% offsets are close to the bottom and top thermocouples

temperatures differences, respectively, for all the heat generation considered. For smaller

pressures, the 90% offset simulation results seem to agree with the measured temperatures

differences for the top thermocouples in the case of Q=100 and 150 W. However, for $Q = 200$W

there is a discrepancy between the measured and simulated results for the same offset and top

thermocouples. For the 70% offset simulations, which corresponds to the bottom

thermocouples and at low pressure, $P < 10000$, there is a good agreement between the measured

and simulated results in case of $Q = 150$ W. However, for the two other heat generation rates, $Q = 100$ W and 200 W, the measured results seem to diverge from the simulated ones, with difference between the two increases as the heat generation increases.

Since the top thermocouples are in better agreement with the 90% offset, this suggests that the top end of the inner cylinder assembly is shifted and it is almost touching the pressure vessel inner walls. Similarly, since the bottom thermocouples are in better agreement with the 70% offset simulated results, at least at high pressures, this supports the possibility that the bottom end has not shifted as much as the top end and therefore the inner cylinder assembly is positioned on an angle inside the pressure vessel.

Regarding all the comments made above for the eccentric case, it seems that the assumption that the inner cylinder assembly is shifted and inclined inside the pressure vessel is founded but cannot be completely confirmed. One way to confirm it is to open the experimental apparatus and check the gap between the inner cylinder assembly and the pressure vessel at both top and bottom ends. However, the process of opening the experiment may lead to a further shift of the inner cylinder assembly and also the estimation of the gap would be very difficult due to its small dimensions. A careful procedure should be created and followed. This will be done when all the possibilities are checked.

4.6. Estimation of the thermal accommodation coefficient

If the assumptions made in the previous two sections are correct, especially the assumption of a shift of the inner cylinder, then the thermal accommodation coefficient could be estimated in the range between 0.3 and 0.4. Further investigation of the reasons leading to the difference between the measured and simulated results in the continuum regime, and the difference between the top, center, and bottom temperatures of the inner cylinder assembly should be performed and may give more information about this discrepancy. A possible redesign of the

support system and better measurements of the inner wall diameter of the pressure vessel may lead to better results.

Chapter V
Conclusion

The long term objective of this research is to contribute to a more accurate prediction of SNF cladding temperatures while undergoing vacuum drying operations. The short term objective of this thesis is to experimentally observe the effect of rarefaction on heat transfer between two coaxial cylinders and to measure the temperature jump and thermal accommodation coefficients between rarefied helium and stainless steel surface in the slip regime. To achieve these objectives three aspects were considered; experimental, numerical, and theoretical.

The experimental aspect of this thesis puts emphasis on the measurement of temperature of the stainless-steel surfaces that are exposed to the helium gas at different levels of rarefaction. By constructing an experiment that was designed from a simple geometry of two coaxial cylinders with a 1 mm annular gap between them, where the rarefied helium was located, temperatures of both cylinders were obtained for a range of pressure and different heat generation rates.

The numerical aspect consisted of creating a geometrically accurate two and three-dimensional CFD models of the experimental apparatus in ANSYS/Fluent to validate the design and to ensure uniform axial temperature and heat flux profiles, along with ensuring that the heat loss from the ends of the coaxial cylinders is minimal.

The theoretical aspect required the derivation of an analytical expression that is used to calculate the temperature jump and thermal accommodation coefficients for a range of pressures and different heat generation rates in the slip regime.

The experimental results were acquired for the measured temperature difference between the inner and outer coaxial cylinders, T_{in} and $T_{out,}$ for a range of pressure from 10^5 Pa to 200 Pa, and for three

different values of heat generation rate, Q=100W, 150W, and 200W. The results demonstrated that an observable rarefaction effect on heat transfer was seen for each of the different heat generation rates. The temperature difference between the cylinders increased as the pressure decreased. Also, the results showed that there was a difference between the measured and simulated temperature differences at high pressures (continuum regime), which was not expected. Many assumptions were made, checked and discussed to explain the reasons of this difference. One possible reason may be an incorrect estimation of the heat losses from the inner cylinder assembly ends. Another reason could be a shift of the inner cylinder assembly inside the pressure vessel, which will make the inner cylinder assembly and the pressure vessel to not be concentric, and the last reason could be an error in the measurement of the diameter of the pressure vessel inner wall. Simulations were performed to check all of the above possibilities. They showed that all of them may have some contribution to the difference. However, the larger contribution was from the shifting of the inner cylinder assembly to where it is inclined inside the pressure vessel. Despite all the assumptions made above, they did not fully explain the reason for this difference. More investigation should be made.

Future considerations for this work should be emphasized on the design of the experiment, namely the size, application of support system, and the calibration of the thermocouples. Initially the size of the experiment allowed for a small aspect ratio to minimize the heat loss from the ends, however this consideration could be revisited so as to implement a smaller apparatus that would be easier to manufacture. Revision for the design of the support structure so as to provide a more robust version would ensure better securement of the inner cylinder assembly inside the pressure vessel, also finding a more appropriate insulation for the ends of the inner cylinder assembly to further minimize the heat loss Lastly, calibrating the thermocouples that were made for the experiment would allow for the elimination of the possibility that the systematic error was a result of the thermocouple readings.

References

[1]   N. Tsoulfanidis, The Nuclear Fuel Cycle, American Nuclear Society, 2013.

[2]   D. B. Rigby, "Evaluation of the Technical Basis for Extended Dry Storage and Transportation of Used Nuclear Fuel," U.S. Nuclear Waste Technical Review Board, 2010.

[3]   NRC (U.S. Nuclear Regulatory Commission), "10, Code of Federal Regulations, Part 72, "Energy: Licensing Requirements for the Independent Storage of Spent Nuclear Fuel and High-Level Radioactive Waste, and Reactor-Related Greater than Class C Waste," Office of Federal Register National Archives and Records Administration, U.S. Government Printing Office, (10 CFR 72)., Washington, DC, 2008.

[4]   U.S. Dept. of Energy, Office of Civilian Radioactive Waste Management (OCRWM), "Characteristics of Spent Nuclear Fuel, High-Level Waste, and Other Radioactive Wastes Which May Require Long-Term Isolation," DOE/RW-0184, 1987.

[5]   Wikid Energy Funhouse (Website). Retrieved from https://wiki.uiowa.edu/display/greenergy/Gunn-Lee-Thorson+Additions+to+Nuclear+Power.

[6]   Foro Nuclear (website). Retrieved from http://www.foronuclear.org/es/ask-the-expert/stages-needed-to-obtain-nuclear-fuel-from-uranium.

[7]   W. Large and R. Sindelar, "Review of Drying Methods for Spent Nuclear Fuel," Westinghouse Savannah River Company, report number WSRC-TR-0075, Savannah River Site, Aiken, SC, 1997.

[8]   NRC, "Cladding Considerations for the Transportation and Storage of Spent Fuel," Interim Staff Guidance Report for the Spent Fuel Project Office of the U.S. NRC, ISG-11 R3, 2003.

[9]   R. Daum, S. Majumdar and M. Billone, "Experimental and Analytical Investigation of the Mechanical Behavior of High-Burnup Zircaloy-4 Fuel Cladding," *J. ASTM Intern.,* vol. 5, no. 5, 2008.

[10]   R. Daum, S. Majumdar, Y. Liu and B. M.C., "Radial-hydride Embrittlement of High-burnup Zircaloy-4 Fuel Cladding," *J. Nucl. Sci. Tech.,* vol. 43, no. 9, pp. 1-14, 2006.

[11]   M. Billone, T. Burtseva and R. Einziger, "Ductile-to-brittle transition temperature for high-burnup cladding alloys exposed to simulated drying-storage conditions," *J. Nucl. Mater.,* vol. 433, pp. 431-448, 2013.

[12]   M. Billone, T. Burtseva and Y. Liu, "Baseline Properties and DBTT of High-Burnup PWR Cladding Alloys," in *Proc. PATRAM*, San Francisco, CA, 2013.

[13]   A. International, "Standard Guide for Drying Behavior of Spent Nuclear Fuel," American Society for Testing and Materials (ASTM) C1553, West Conshohocken, PA, 2008.

[14]   NRC, "Standard Review Plan for Spent Fuel Dry Storage Systems at a General License Facility — Final Report," U.S. Nuclear Regulatory Commission, NUREG-1536, Revision 1, Washington, DC, 2010.

[15]   S. A. Schaaf and P. L. Chambre, Flow of Rarefied Gases, New Jersey: Princeton University Press, 1961.

[16]   F. Sharipov and D. Kalempa, "Velocity Slip and Temperature Jump Coefficients for Gaseous Mixtures. IV. Temperature jump coefficient," *International Journal of Heat and Mass Transfer,* vol. 48, pp. 1076-1083, 2005.

[17]   J. C. Maxwell, "On stress in rarefied gases arising from inequalities of temperature," *Phil.Trans. R. Soc. Lond.,,* vol. 170, p. 231–256, 1878.

[18]   F. O. Goodman, "Thermal accommodation," *Progress in Surface Science,* vol. 5, no. 3, pp. 261-375, 1974.

[19]   W. M. Trott, J. N. Castañeda, J. R. Torczynski, M. A. Gallis and D. J. Rader, "An experimental assembly for precise measurement of thermal accommodation," *Review of scientific instruments,* vol. 82, no. 035120, 2011.

[20]   H. Yamaguchi, K. Kanazawa, Y. Matsuda, T. Niimi, A. Polikarpov and I. Graur, "Investigation on heat transfer between two coaxial cylinders for measurement of thermal accommodation coefficient," *Physics of Fluids,* vol. 24, no. 062002, 2012.

[21]   F. O. Goodman, "Thermal Accommodation Coefficients," *J. Phys. Chem.,* vol. 84, pp. 1431-1445, 1980.

[22] S. Song and M. M. Yovanovich, "Correlation of thermal accommodation coefficient for 'engineering' surfaces," in *Proceedings of the Twenty-fourth ASME National Heat Transfer Conference*, Pittsburg, PA, 1987.

[23] M. Billone, T. Burtseva and R. Einziger, "Ductile-to-brittle transition temperature for high-burnup cladding alloys exposed to simulated drying-storage conditions," *J. Nucl. Mater.,* vol. 433, pp. 431-448, 2013.

[24] M. Hadj-Nacer, "Tangential momentum accommodation coefficient in microchannels with differebt surface materials (measurement and simulations)," PH.D Thesis, University of Aix-Marseille, 2012.

[25] L. Loeb, Kinetic Theory of Gases, 2nd Edition, McGraw-Hill Book Company Inc., 1934.

[26] M. S. Smoluchowski, "On conduction of heat by rarefied gases," *Philosophical Magazine Series 5,* vol. 46, no. 279, 1898.

[27] E. H. Kennard, Kinetic Theory of Gases, New York: McGraw-Hill Book Company, Inc., 1938.

[28] P. Welander, "The temperature jump in a rarefied gas.," *Arkiv foer Fysik,* vol. 7, no. 44, p. 507–553, 1954.

[29] J. T. Lin and D. R. Willis, "Kinetic Theory Analysis of Temperature Jump in a Polyatomic Gas," *Phys. Fluids,* vol. 15, p. 31, 1972.

[30] D. Maharjan, M. Hadj-Nacer, and M. Ho. "Simulation of heat transfer across rarefied gas in annular and planar geometries: comparison of Navier-Stokes, s-model and DSMC methods results," In proceed of ASME International Conference on Nanochannels, Microchannels, and Minichannels, San Francisco, CA, USA 2015.

[31] Y. T. Hsia and G. A. Domoto, "An experimental investigation of molecular rarefaction effects in gas lubricated bearings at ultra low clearances," *Journal of Lubrication,* vol. 105, no. 1, pp. 120-130, 1983.

[32]   Y. Mitsuya, "Modified Reynolds equation for ultra-thin film gas lubrication using 1.5 order slip flow model and considering surface accommodation coefficient," *Journal of Tribology,* vol. 115, no. 2, p. 289–294, 1993.

[33]   D. A. Lockerby, J. M. Reese, D. R. Emerson and R. W. Barber, "Velocity boundary at solid walls in rarefied gas calculations," *Physical Review E,* vol. 70, no. 1, 2004.

[34]   F. Sharipov and V. Seleznev, "Data on internal rarefied gas flows," *J. Phys. Chem. Ref. Data,* vol. 27, no. 3, pp. 657-706, 1998.

[35]   C. Cercignani and A. Daneri, "Flow of a rarefied gas between two parallele plates," *Phys. Fluids,* vol. 6, pp. 993-996, 1963.

[36]   Hadj-Nacer M., Manzo T., Ho M., Graur I., and M. Greiner "Phenomena Affecting Used Nuclear Fuel Cladding Temperatures During Vacuum Drying Operations," *in ANS Conference 2015 International High-Level Radioactive Waste Management,* Charlotee, NC, April 2015.